The Response of Extratropical Cyclone Propagation in the Northern Hemisphere to Global Warming

ALEX D. CRAWFORD,[a] MICHELLE R. MCCRYSTALL,[a] JENNIFER V. LUKOVICH,[a] AND JULIENNE C. STROEVE[a,b,c]

[a] *Centre for Earth Observation Science, University of Manitoba, Winnipeg, Manitoba, Canada*
[b] *Department of Earth Sciences, University College London, London, United Kingdom*
[c] *National Snow and Ice Data Center, Cooperative Institute for Research in Environmental Science, University of Colorado Boulder, Boulder, Colorado*

(Manuscript received 9 February 2023, in final form 20 July 2023, accepted 20 July 2023)

ABSTRACT: Extratropical cyclones (ETCs) are a common source of natural hazards, from heavy rain to high winds, and the direction and speed of ETC propagation influence where impacts occur and for how long. Eighteen models from phase 6 of the Coupled Model Intercomparison Project (CMIP6) are used to examine the response of Northern Hemisphere ETC propagation to global warming. In winter, simulations show that ETCs become slower over North America and the Arctic but faster over the Pacific Ocean and part of Europe. In summer, storm propagation becomes slightly slower throughout much of the midlatitudes (30°–60°N). Trends in both seasons relate closely to the impact of global warming on upper-level (250 hPa) winds and the 850–250-hPa thickness gradient. Wherever local thickness gradients weaken in the future, ETCs travel more slowly; conversely, wherever they strengthen, ETCs travel more quickly. In contrast to past work, we find that winter storm propagation becomes more zonal over the Pacific and Atlantic Oceans, which may link to decreased atmospheric blocking and less-sinuous flow at 500 hPa. The importance of model projections of the 850–250-hPa thickness gradient for meridionality of ETC propagation remains uncertain for these regions. However, for North America, models that project stronger thickness gradients also project less-sinuous flow and more-zonal ETC propagation. Overall, this work highlights strong regional variation in how the speed and direction of ETC propagation, and the upper-level circulation patterns that govern them, respond to continued warming.

SIGNIFICANCE STATEMENT: Extratropical storms are common sources of natural hazards like heavy rain and high winds. In our analysis of projections from 18 climate models, we find that winter storms tend to move more slowly over midlatitude North America and the Arctic as the world warms but move faster over the North Pacific Ocean and part of Europe. Slight slowing of summer storms is projected throughout much of the midlatitudes. When storms move slower, their attendant hazards (like heavy precipitation) last longer for the areas they impact. Further, Atlantic winter storms travel more west to east instead of southwest to northeast, so they impact Iceland less often and the British Isles more often. Changes become more dramatic with each additional degree of global warming.

KEYWORDS: Atmosphere; Northern Hemisphere; Atmospheric circulation; Extratropical cyclones; Model comparison

1. Introduction

Synoptic-scale extratropical cyclones (ETCs) are responsible for many of the heavy precipitation days, high wind events, and large temperature swings in the middle and high latitudes (e.g., Roberts et al. 2008; Hewson and Neu 2015; Crawford et al. 2020). Faster propagation can enhance a storm's maximum wind speed; however, it also decreases the time a storm spends over any given location, which decreases the duration of any impact associated with the storm. Slower propagation, by contrast, prolongs exposure, so cumulative impacts (e.g., total precipitation) may be worse for slower storms, all else being equal (e.g., precipitation rate or storm size). This relationship is better recognized for tropical cyclones, and several studies have examined whether tropical cyclone propagation speed has slowed in response to global warming (Kossin 2018; Chan 2019; Yamaguchi et al. 2020; Sun et al. 2021).

Using global and regional climate models, recent studies have identified changes in ETCs in response to global warming, which will in turn affect weather in the middle to high latitudes. For example, a common response of ETCs to global warming in modeling experiments is a reduction in ETC frequency and/or poleward shift of the main oceanic storm tracks in the North Atlantic and North Pacific in both winter and summer (Ulbrich et al. 2009; Eichler et al. 2013; Harvey et al. 2020; Priestley and Catto 2022).

Despite ample research regarding storm frequency and intensity, the direction and speed with which ETCs travel has received little attention. In aquaplanet experiments with induced global warming of 4°C, part of the poleward shift in the tracks of intensifying ETCs was attributed to more latitudinal

Denotes content that is immediately available upon publication as open access.

Supplemental information related to this paper is available at the Journals Online website: https://doi.org/10.1175/JCLI-D-23-0082.s1.

Corresponding author: Alex Crawford, alex.crawford@umanitoba.ca

DOI: 10.1175/JCLI-D-23-0082.1

(i.e., meridional) storm displacement (Tamarin and Kaspi 2017). This implies that even if ETC genesis regions did not shift with warming, the influence of ETCs would still tend to shift poleward with warming. In the Northern Hemisphere, the presence of large midlatitude landmasses disrupts these storm tracks; however, CMIP5 models do show a tilt of the Pacific and Atlantic storm tracks toward more poleward (meridional) ETC propagation under the RCP8.5 scenario (Tamarin-Brodsky and Kaspi 2017).

Also uncertain is whether the speed of ETC propagation changes in a warming world. Various studies have reported longer duration weather anomalies associated with more persistent circulation patterns (Pfleiderer et al. 2019; Francis et al. 2020; Li and Thompson 2021). If weather patterns do become more persistent as the world warms, this likely would occur in conjunction with slower-propagating ETCs. However, one study only found increased persistence of weather patterns in certain regions in summer (Pfleiderer et al. 2019) and another reported an overall lack of trends in circulation (wind pattern) persistence over central Europe in summer and winter (Huguenin et al. 2020). Both studies used a subset of CMIP5 models.

Kornhuber and Tamarin-Brodsky (2021) directly examined ETCs and found that summer ETCs (and other weather patterns) propagate faster in places where 500-hPa winds become faster (and propagate slower where 500-hPa winds become slower) in CMIP5 simulations of future warming. Slowing of ETC propagation was more common (especially in Eurasia) for models that projected weakening of the midlatitude to Arctic temperature gradient. Still, we do not know whether these same relationships hold for ETCs in winter, when their impact on midlatitude weather is strongest. Moreover, past research has shown that newer CMIP6 models provide a more accurate portrayal of ETCs than CMIP5, in part because of finer horizontal resolution (Harvey et al. 2020; Priestley et al. 2020; Song et al. 2021), so results may differ from CMIP5. This study builds on past work (e.g., Tamarin-Brodsky and Kaspi 2017; Kornhuber and Tamarin-Brodsky 2021) by presenting a more comprehensive examination of ETC propagation speed and direction in both winter and summer in 18 climate models from the CMIP6 archive (Table S1 in the online supplemental material) and ERA5 reanalysis, while also accounting for differences in horizontal resolution. Three questions are addressed:

1) What is the seasonality of the relationship between global warming and the speed and direction of ETC propagation?
2) Do results from CMIP6 confirm or refute prior work with other models?
3) How strongly does any such response to warming depend on changes to large-scale circulation patterns (e.g., the polar jet stream) and the atmosphere's local and regional thermal structure?

2. Methods

a. Datasets

We use 18 models participating in Phase 6 of the Coupled Model Intercomparison Project (CMIP6; Eyring et al. 2016) that all have 6-h sea level pressure (SLP) fields available for both the Historical (1850–2014) and SSP5-8.5 (2015–2100) experiments. SSP5-8.5 represents a "shared socioeconomic pathway" with high emissions and a radiative forcing of roughly 8.5 W m^{-2} at 2100. SSP5-8.5 was chosen over other experiments because 1) the necessary data were available for more models and 2) it covers the widest range of global annual temperature increases. Since only two models had at least three ensemble members available, only the first member was used from each model. Additional variables include average daily fields of zonal and meridional wind and geopotential height at multiple pressure levels, and monthly fields of temperature at multiple levels, including the near surface. In cases in which these additional variables were only available at 6-h resolution, they were averaged to daily fields before other computations. Geopotential height was unavailable at the daily or subdaily resolution for three models: BCC-CSM2-MR, KIOST-ESM, and NESM3. Models are distinguished as "high resolution" if their nominal spatial resolution is 100 km or finer (Table S1 in the online supplemental material).

Historical CMIP6 data are compared with the fifth major global reanalysis produced by ECMWF (ERA5) for the period 1979–2014 (Hersbach et al. 2020). ERA5 data were downloaded at a 0.25° spatial resolution (Hersbach et al. 2018). Wind and geopotential height data were downloaded at an hourly temporal resolution and averaged to daily fields. Data for SLP (every 6 h) and temperature (monthly) already matched the CMIP6 temporal resolution.

b. Cyclone detection and tracking

The algorithm used for ETC detection and tracking is described in detail in past work (Crawford and Serreze 2016). For both ERA5 and CMIP6, every SLP field is regridded to a 100 km by 100 km grid with a pole-centered Lambert's azimuthal equal-area projection. This resolution is in the middle of the CMIP6 models, and finer resolutions have been shown to yield only minor differences across the Northern Hemisphere (Crawford et al. 2021). Although area is preserved in this projection, shape is not, with distortion highest at lower latitudes (up to ±10% in the width or height of a grid cell at 40°N).

Cyclone centers are identified as grid cells that meet the following criteria:

1) SLP is lower than all neighboring cells (cells within 200 km x or y distance),
2) elevation is no higher than 1500 m, and at least 60% of neighboring cells are also below 1500-m elevation, and
3) SLP is at least 7.5 hPa lower than the average for all cells 900–1000 km away.

The highest closed isobar that encompasses only one cyclone center and no SLP maximum is the initial measure of cyclone area. However, if 1) two cyclone centers lie within 1200 km of each other and 2) merging them would at least double the area of the larger cyclone, they are combined into a multicenter cyclone. Cyclone tracks are continued across each 6-h interval by first using past propagation to predict the

next location of a cyclone. The closest cyclone center to that predicted location in the subsequent SLP field is identified as the continuation of a cyclone track so long as propagation speed does not exceed 150 km h^{-1}. If no cyclone center is close enough in the subsequent SLP field, the cyclone track ends.

Cyclone propagation is recorded for each 6-h observation based on the meridional and zonal distance the cyclone traveled since the previous observation. Meridionality (M) of cyclone propagation at each 6-h observation is defined using Eq. (1), where u is zonal propagation and v is meridional propagation:

$$M = \frac{v^2}{u^2 + v^2}. \quad (1)$$

This is equivalent to the absolute value of the meridional circulation index used in past studies (Francis and Vavrus 2015; Blackport and Screen 2020). Values of 0%–50% indicate primarily zonal direction, and values of 50%–100% indicate primarily meridional direction.

Calculation of aggregate ETC statistics is performed only on cyclones that 1) travel over 24 h and 1000 km and 2) are observed at least once in a grid cell with a surface elevation of 500 m or less. Because cyclones can pass through multiple grid cells in one 6-h period, cyclone locations are interpolated to a 1-h resolution before calculating track density (the number of unique cyclone tracks per area per time period), following Zolina and Gulev (2002).

c. *Defining atmospheric parameters*

The speed and meridionality of ETC propagation are compared with daily fields of upper-level (250 hPa) wind speed and meridionality [again using Eq. (1)] by masking the wind characteristics to within 600 km of ETC centers before calculating seasonal averages. To link variability in upper-level winds to the thermal structure of the atmosphere, the magnitude of the gradient of the 850–250-hPa thickness is computed locally (i.e., discrete differencing of the eight nearest neighbors of each grid cell north of 30°N). Although prior studies have used atmospheric thickness extending down to 1000 hPa (e.g., Francis and Vavrus 2012, 2015), we limit ourselves to 850 hPa because in some CMIP6 models the geopotential height at 1000 hPa is masked if the surface pressure is less than 1000 hPa. For two figures, a large-scale (regional) thickness difference is also calculated, subtracting average Arctic thickness (60°–90°N) from average midlatitude thickness (30°–60°N).

The strength of the relationship between storm propagation and environmental winds is slightly weaker, especially over the Arctic Ocean, if 500-hPa winds are used instead of 250-hPa winds (see Fig. S1 in the online supplemental material). If a larger aggregation radius around ETC centers is used, the correlations between wind characteristics and the local 850–250-hPa thickness gradient become stronger (Figs. S2 and S3 in the online supplemental material), but the correlations between wind characteristics and either ETC propagation characteristic become weaker (Figs. S4 and S5 in the online supplemental material). Using 600 km as an aggregation radius provides a balance between these opposing sensitivities. Sensitivity to aggregation radius is minor for wind speed but notable for wind meridionality. Only the magnitude of correlations is affected, not the sign.

Two methods are used to identify atmospheric blocking events, following the "absolute" and "anomaly" methods outlined by Woollings et al. (2018), to which readers are referred for details. Briefly, the absolute method identifies areas greater than 500 000 km^2 for which the poleward gradient in 500-hPa geopotential height is positive, but it is restricted to between 45° and 70°N latitude. The anomaly method uses daily anomalies (with respect to the daily mean 1979–2014) of 500-hPa geopotential height. Blocking is defined as areas (at any latitude) of at least 2 million km^2 for which all grid cells exceed the 90th percentile of anomalies within 50°–80°N in the climatological period.

Sinuosity of 500-hPa flow is defined following Cattiaux et al. (2016) and Blackport and Screen (2020). For each day, the average 500-hPa geopotential height between 30° and 70°N was identified. Next, the total length of the isohypse corresponding to that value (including any cutoffs) was calculated. The ratio of isohypse length to the length of the 50th parallel is the sinuosity. Higher values indicate more waviness.

In this paper "global warming" refers to the trend in the global annual surface air temperature anomaly relative to 1850–1900, following the IPCC (2021). Arctic amplification is defined as the ratio of the trend in Arctic warming (60°–90°N) to the global trend following Hahn et al. (2021). Correlations between ETC propagation and either upper-level winds or thickness gradients for the reference period (1980–2014) are measured using Spearman's rho, with two-tailed p values estimated using a Student's t distribution. Ordinary least squares regression is used to calculate trends relative to time and global annual temperature anomaly (1980–2099). To ensure robust results, comparisons are only made using grid cells with at least 10 ETC passages for each of at least 20 years.

3. Results

a. *Validation of high- and low-resolution CMIP6 models using ERA5*

In ERA5, the areas where winter ETCs move fastest are also areas of substantial cyclogenesis: along the western and southern flanks of the North Atlantic and North Pacific Ocean storm tracks, the lee of the northern/central Rocky Mountains, and northern China (Fig. 1b). ETC meridionality is nearly always less than 50%, reflecting ETCs' preferentially zonal propagation. Propagation is more meridional around topographic barriers, such as Greenland and the Alaska Range (Fig. 1c).

Biases observed in CMIP6 models are consistent with studies using other cyclone detection and tracking algorithms (Zappa et al. 2013; Harvey et al. 2020; Priestley et al. 2020). Winter ETC activity is underestimated throughout most of the Northern Hemisphere in the low-resolution CMIP6 multimodel mean (Fig. 1d) except along the southern flank of the North Atlantic–European storm track, where track density is too high. In high-resolution models, the track density bias is much reduced, especially over the Arctic and Pacific Oceans

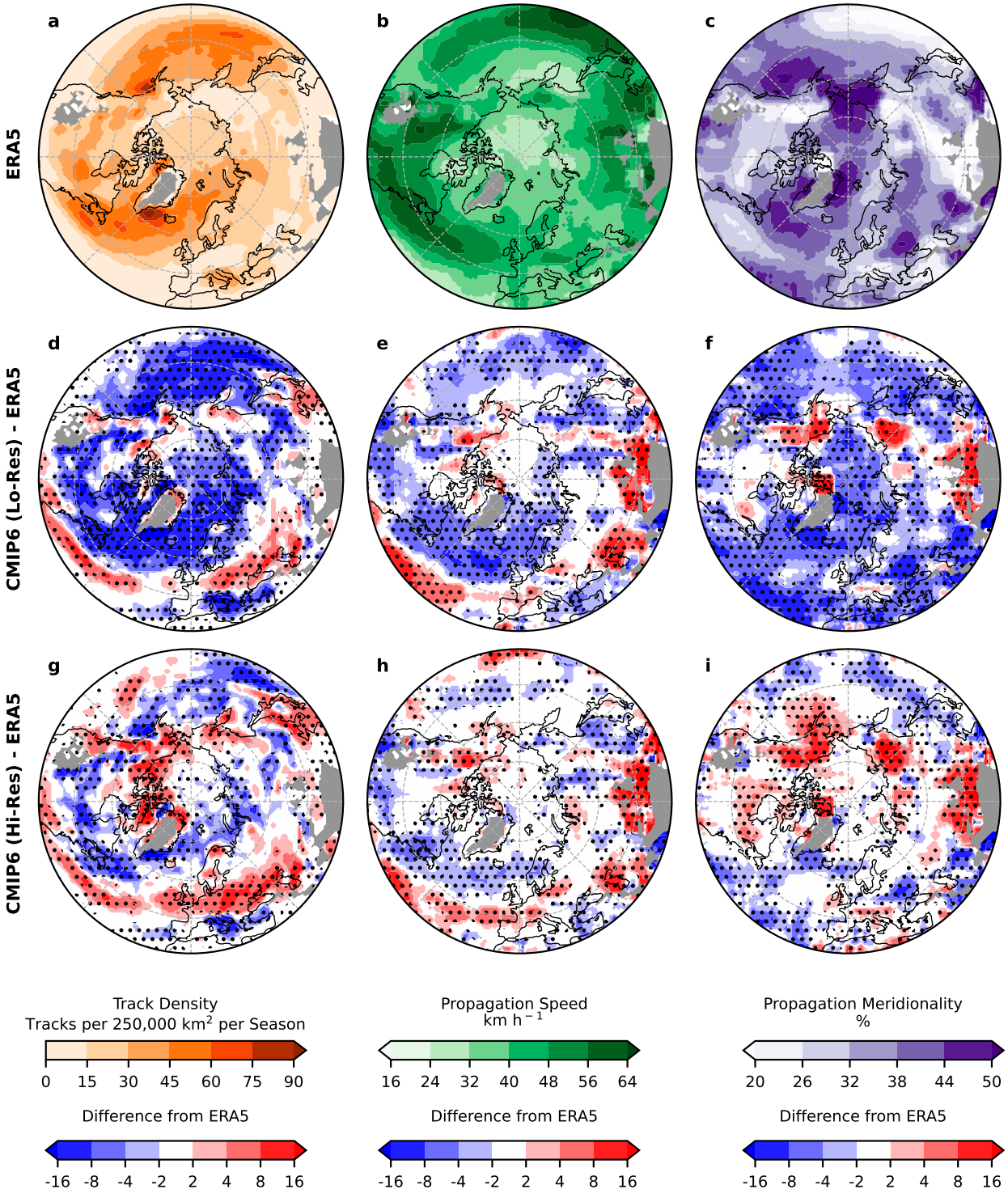

FIG. 1. Comparison of winter CMIP6 ETC characteristics with ERA5: Shown are ETC (left) track density, (center) propagation speed, and (right) propagation meridionality (a)–(c) averaged for winter (December–February) 1980–2014 using ERA5, along with (d)–(f) the multimodel mean for 10 low-resolution models minus ERA5 results and (g)–(i) the multimodel mean for eight high-resolution models minus ERA5 results. Stippling indicates that at least 80% of models agree on the sign of the coefficient. Gray shading indicates no data.

(Fig. 1g; Song et al. 2021). However, the North Atlantic–European storm track is still too zonal and slightly too far south.

ETCs in the main winter Atlantic storm track are slower in CMIP6 models than in ERA5, except on the storm track's southern flank (Figs. 1e,h). The bias in ETC propagation speed is reduced by about one-half in high-resolution models relative to low-resolution models for both the North Atlantic and North Pacific. ETC propagation in low-resolution models is almost ubiquitously too zonal (Fig. 1f), but biases are smaller and more spatially varied in high-resolution models (Fig. 1i). In the high-resolution models, ETC propagation is too zonal (blue shading) in the main oceanic storm tracks and too meridional (red shading) over Canada and at the eastern end of the Pacific storm track. An excessively zonal Atlantic storm track is a common finding of previous work with CMIP6 and earlier models, likely caused by unrealistic diabatic processes, low grid resolution, and biases in blocking and surface temperatures (Keeley et al. 2012; Zappa et al. 2013; Harvey et al. 2020; Priestley et al. 2020; Schemm 2023).

Relative to winter ETCs, summer ETCs are fewer in number and travel both more slowly and more zonally (Figs. 2a–c). The fastest propagation regions for the oceanic storm tracks shift from the western edges of the ocean basins to the central regions, and to the south. Biases in track density for CMIP6 models are similar in magnitude between winter and summer, but since there are fewer storms in summer, the relative biases are greater (Figs. 2d,g). Both low- and high-resolution models depict too few storms over the Arctic Ocean, consistent with past studies (Zappa et al. 2013; Akperov et al. 2019; Song et al. 2021). ETC frequency is underestimated in the midlatitude Atlantic and Pacific Oceans, and overestimated over the midlatitude continents, with low-resolution models more likely to show underestimation (Priestley et al. 2020; Harvey et al. 2020; Song et al. 2021). Propagation speed bias is small in the areas of highest track density in summer, but where there is bias (e.g., over Siberia) storms in CMIP6 models generally propagate too slowly. Low-resolution models also have a strong zonal propagation bias throughout the Northern Hemisphere in summer. As in winter, this bias is much reduced in high-resolution models.

In summary, high-resolution models are demonstrably better matches for ERA5 track density and storm propagation than low-resolution models in both seasons and are therefore better suited for projecting future ETC propagation [see also Priestley et al. (2020) or Song et al. (2021)]. Recall that we reproject all data to a common grid before ETC detection, so the better performance by the eight high-resolution models is not simply a gridding issue. Therefore, only the multimodel mean of those high-resolution models (Table S1 in the online supplemental material) is shown in Fig. 3 and in Figs 5, 6, and 8, described in more detail below.

b. *Storm propagation in a warming world*

As the world warms, ETC frequency in the Northern Hemisphere declines overall. (Fig. 3). In winter, declining track density in the Pacific (30°–45°N) combined with smaller increases to track density over eastern Asia and the Bering Sea represent a weakening and poleward shift in the main storm track. In the North Atlantic, declines over the Icelandic low region combined with smaller increases near the British Isles represent a weakening and equatorward shift of the main storm track (Fig. 3a). In summer, increasing track density is greatest along the east side of Greenland—a poleward shift of the Atlantic storm track (Fig. 3d)—and track density declines throughout the continents and Pacific. The winter Atlantic results differ from earlier models (Ulbrich et al. 2009) but are consistent with other work using CMIP6 (Harvey et al. 2020). The general weakening and poleward shift in the Pacific are consistent with past work (e.g., Crawford and Serreze 2017; Harvey et al. 2020; Priestley and Catto 2022), as are the declines in ETC frequency over Canada in both seasons (Chang 2013; Eichler et al. 2013; Eichler 2020; Harvey et al. 2020) and over the Mediterranean Sea region in winter (Pinto et al. 2007; Raible et al. 2008; Ulbrich et al. 2009; Eichler et al. 2013).

Declines in ETC frequency co-occur with slower propagation in many places, but not all. In winter, storm propagation becomes faster in the western and central Pacific but slower in most other places, including the eastern Pacific, North America, and the periphery of the Arctic Ocean (Fig. 3b). Results are less clear for the Atlantic storm track, with propagation speed increasing from 30° to 50°N but decreasing in the Nordic seas. Additionally, propagation direction in both the Atlantic and Pacific storm tracks becomes more zonal in winter, with mixed regions of opposite tendency over the continents (Fig. 3c). Only minor changes occur for storm propagation in summer, with slowing dominant south of 60°N (Fig. 3e), which is consistent with previous descriptions of the weather pattern response (Kornhuber and Tamarin-Brodsky 2021). Also in summer, a west-to-east band between about 45° and 60°N shows more-zonal propagation over North America and the Atlantic but more-meridional propagation over Eurasia (Fig. 3f).

Our result that winter ETCs over the Pacific and Atlantic trend toward more-zonal propagation differs from past work showing more poleward displacement for such storms under a warming scenario in CMIP5 models (Tamarin-Brodsky and Kaspi 2017). There are several methodological differences between the studies: We examine the local (cellwise) ratio between zonal and meridional propagation for all storms, whereas Tamarin-Brodsky and Kaspi (2017) examine the trackwise latitudinal displacement (i.e., the latitude of the point of maximum intensity in a ETC track minus its genesis latitude). They also limit their analysis to deepening storms within particular regions. For the Pacific, the area where propagation becomes more zonal only intersects the northern edge of the study area used by Tamarin-Brodsky and Kaspi (2017), which may alone explain the differences.

However, the differences in the Atlantic are more difficult to reconcile. Replicating Tamarin-Brodsky and Kaspi's (2017) trackwise methods yields no consistent latitudinal displacement for either basin but a tendency for more-longitudinal displacement in most CMIP6 models in the Atlantic (Fig. 4f). Different tracking algorithms are used in each study, but results diverge farther if examining only the storms in the upper 50th or 75th percentile of intensity (Figs. S6 and S7 in the online supplemental material), for which different tracking

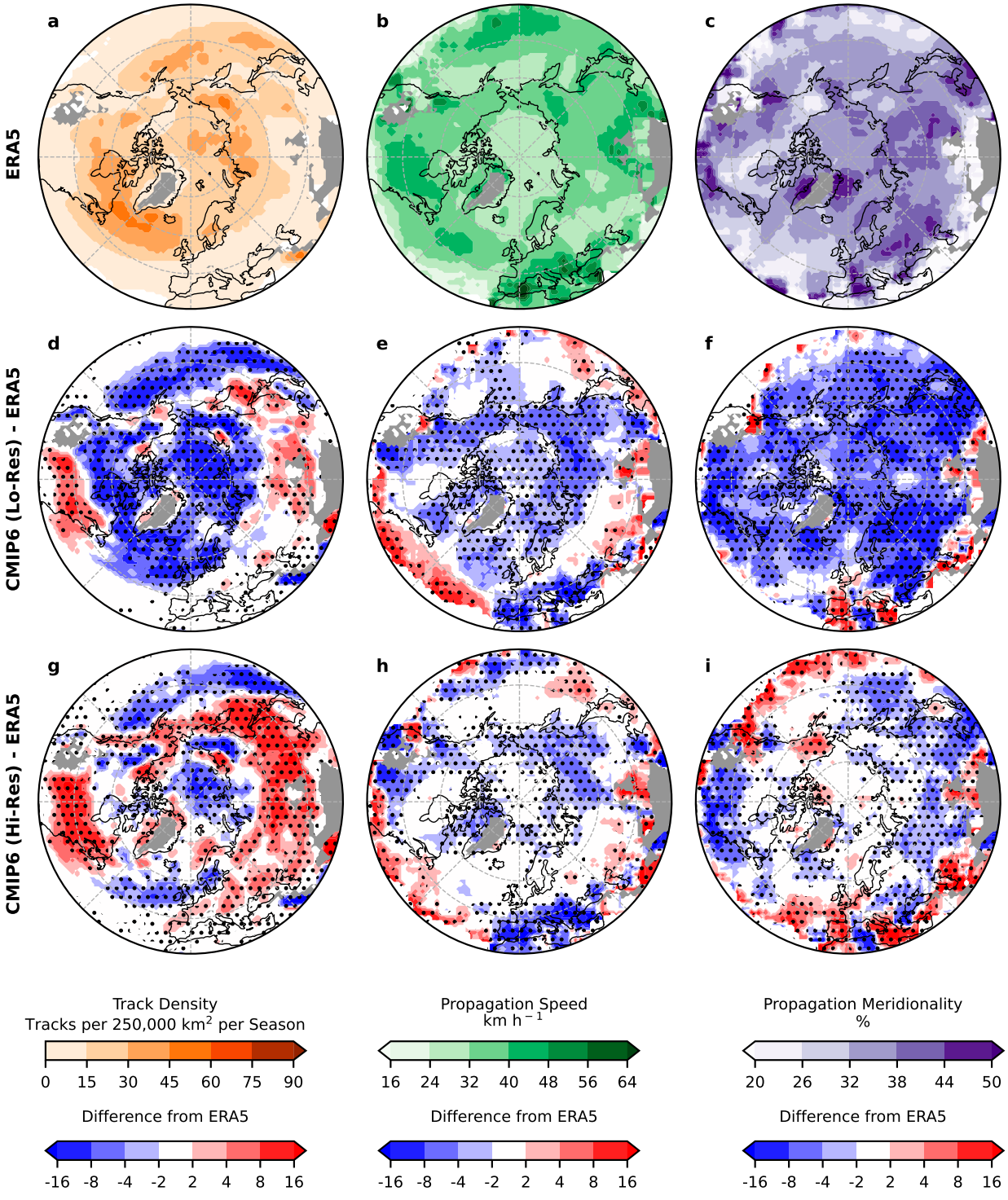

FIG. 2. Comparison of summer CMIP6 ETC characteristics with ERA5: as in Fig. 1, but for summer (June–August).

algorithms show stronger agreement (Neu et al. 2013). Therefore, this likely represents a difference between CMIP5 and CMIP6. Indeed, CMIP6 models show greater reductions in ETC frequency on the poleward flank of the Atlantic storm track than CMIP5 or CMIP3 models [see Fig. 3 in Harvey et al. (2020)]. This is consistent with CMIP6 models being less likely to show a trend toward more poleward displacement of ETCs than their predecessors.

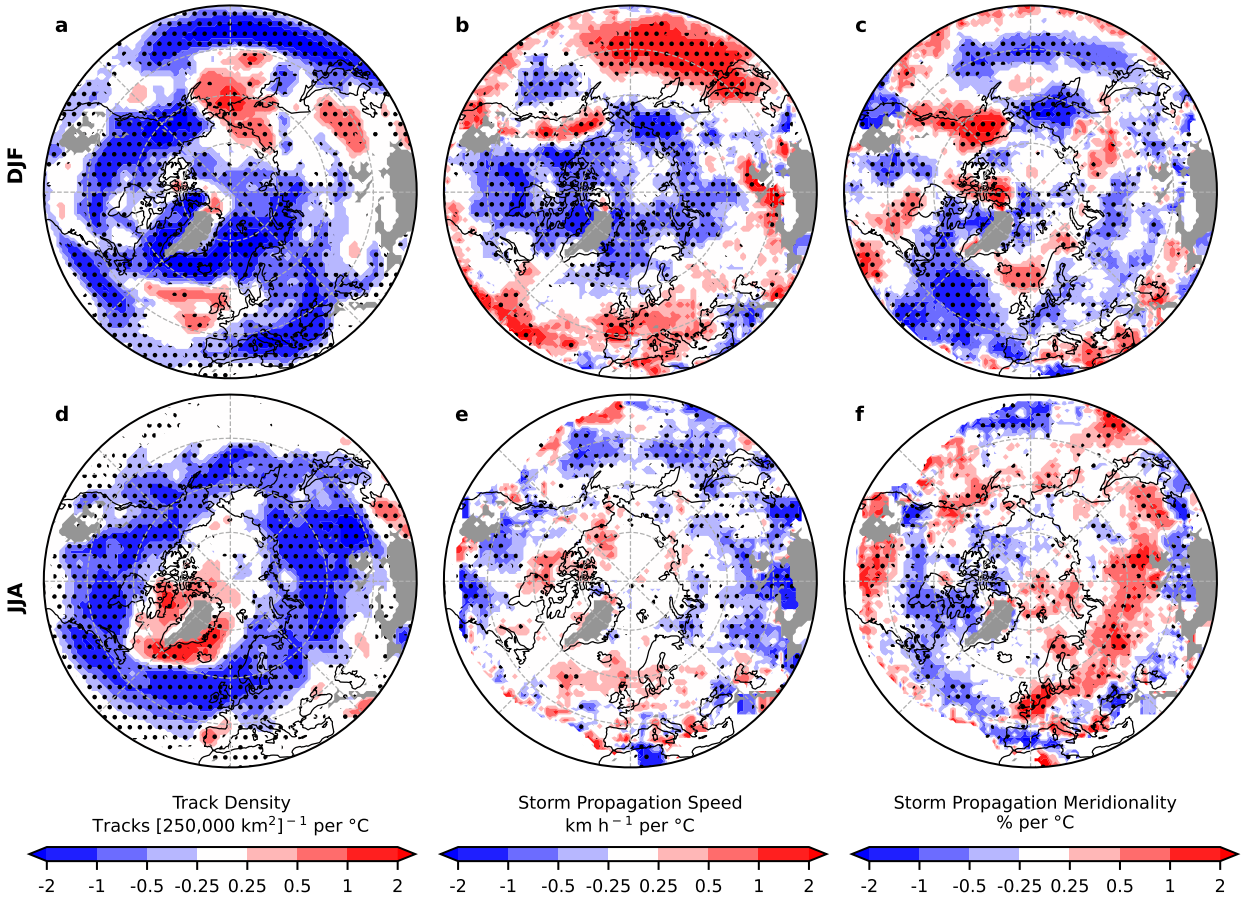

FIG. 3. Regression coefficients for (a)–(c) winter and (d)–(f) summer ETC characteristics regressed on global annual temperature anomaly in Historical+SSP5-8.5 simulations of the eight high-resolution CMIP6 models (1980–2099). Stippling indicates that at least 80% of models agree on the sign of the coefficient. Gray shading indicates no data.

c. ETC propagation and the thermal wind relationship

Historically (1980–2014), the speed and direction of ETC propagation is strongly correlated to the 250-hPa wind (Fig. 5, left). Faster jet-stream-level wind speeds within 600 km of an ETC are associated with faster ETC propagation in all regions, seasons, and datasets. Correlations are stronger in winter than summer and stronger in ERA5 than the CMIP6 multimodel mean. The meridionality of 250-hPa winds also positively correlates with meridionality in ETC propagation, although correlations are weaker for meridionality than speed. As with wind and propagation speed, correlations for meridionality are greater in winter, when 250-hPa winds are stronger.

Upper-level wind speed is strongly controlled by thermal wind shear, represented here as the average local gradient in daily 850–250-hPa thickness (Fig. 5, right). As with upper-level winds and ETC propagation, the positive correlation between upper-level wind speed and thickness gradients is stronger in winter than in summer and stronger in the midlatitudes than in the Arctic. Throughout most of the midlatitudes in winter, correlations for wind speed exceed 0.75 in both ERA5 and CMIP6 models (Figs. 5c,g). Stronger gradients in 850–250-hPa thickness are generally associated not only with faster 250-hPa winds, but also more-zonal 250-hPa winds in both ERA5 and CMIP6 models. However, correlations are much weaker for wind meridionality than for wind speed, and significant relationships are less widespread—especially in ERA5 in summer.

Additionally, both ERA5 and CMIP6 show that, around eastern Siberia (125°E–180°) in winter, stronger thickness gradients are associated with more-meridional winds, in contrast to most of the Northern Hemisphere (Figs. 5d,h). Over most of the Northern Hemisphere, the average winter thickness gradient is south to north, so strengthening that gradient enhances primarily westerly winds aloft. In eastern Siberia, by contrast, the gradient is east to west, with the lower thickness values lying over the cold Siberian high (Fig. S8 in the online supplemental material). As a result, this is one of only two regions (along with Baffin Bay) for which the average wind at 250 hPa is more meridional than zonal, and strengthening the thickness gradient enhances primarily southerly winds aloft.

In summary, CMIP6 models reproduce the observed thermal wind relationship whereby stronger local gradients in 850–250-hPa thickness (and therefore tropospheric density) generate faster and more-zonal winds at 250 hPa. They also

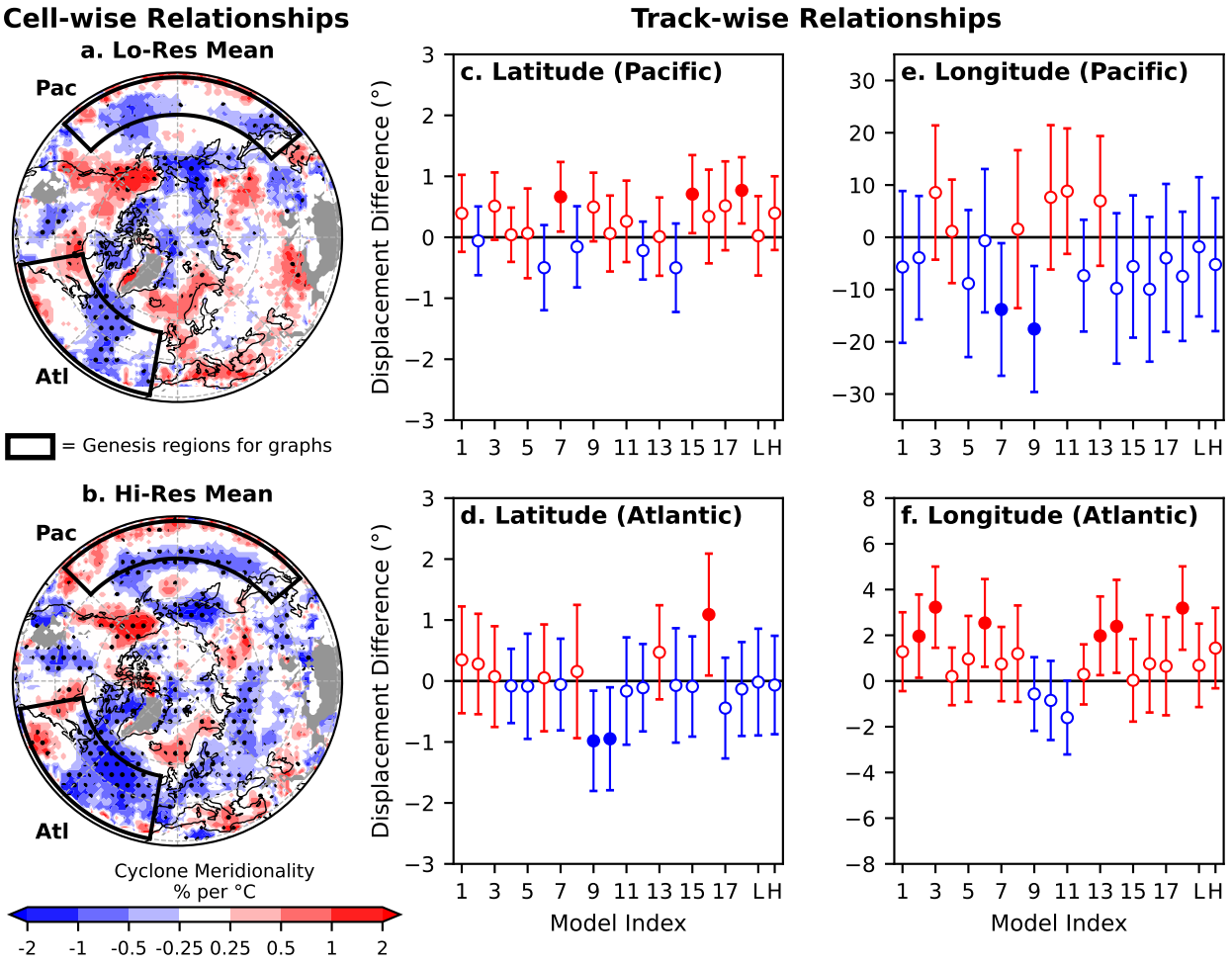

FIG. 4. Comparison of cellwise and trackwise change with the meridionality of cyclone propagation: Maps of the cellwise relationship between the meridionality of cyclone propagation and annual global temperature anomaly in (a) low-resolution and (b) high-resolution CMIP6 models (1980–2099). Also shown is the difference in average track displacement of December–February ETCs in the (c),(e) Pacific and (d),(f) Atlantic regions in 2080–99 minus 1980–99. "Displacement" is defined following Tamarin-Brodsky and Kaspi (2017) as the latitude/longitude of the point of maximum intensity minus the latitude/longitude of cyclogenesis, for Pacific and Atlantic ETCs. Intensity is measured as the maximum Laplacian of central pressure. The difference of the averages (dots) and 95% confidence interval (using Welch's *t* test; whiskers) for these periods were calculated in each model (See Table S1 in the online supplemental material for the model names listed by index number) and in the low-resolution (label L) and high-resolution (label H) multimodel means. Whiskers for the multimodel means are derived via propagation of uncertainty. Solid dots indicate significant differences at a 95% confidence level.

reproduce the general spatial and seasonal correlation patterns between upper-level winds and ETC propagation speed and meridionality, although in this case CMIP6 models generally show weaker relationships than ERA5. Therefore, it is reasonable to expect that future changes to ETC propagation projected in Fig. 3 are controlled by changes in upper-level winds and thermal wind shear.

d. Controls on the speed of ETC propagation

1) LOCAL UPPER-LEVEL WINDS AND THICKNESS GRADIENTS

With ETC propagation speed so strongly determined by the strength of upper-level winds, it is unsurprising that the response of ETC propagation to global warming closely aligns with the response of the 250-hPa wind and, by the thermal wind relationship, the local 850–250-hPa thickness gradient (Fig. 6). Throughout most of the midlatitudes, the thickness gradient increases in winter. The northwestern and southeastern North Pacific, where this gradient intensification is especially strong (Fig. 6a), also see the greatest increase in 250-hPa wind speed (Fig. 6b) and therefore ETC propagation speed (Figs. 3b/6c). Similarly, weakening of the 250-hPa winds and slowing of ETC propagation occurs where the thickness gradient weakens (e.g., the Greenland Sea and western Canada).

In summer, the response of thickness gradients to global annual warming is largely inverted, with weakening in the midlatitudes and strengthening north of 60°N (Fig. 6d). This

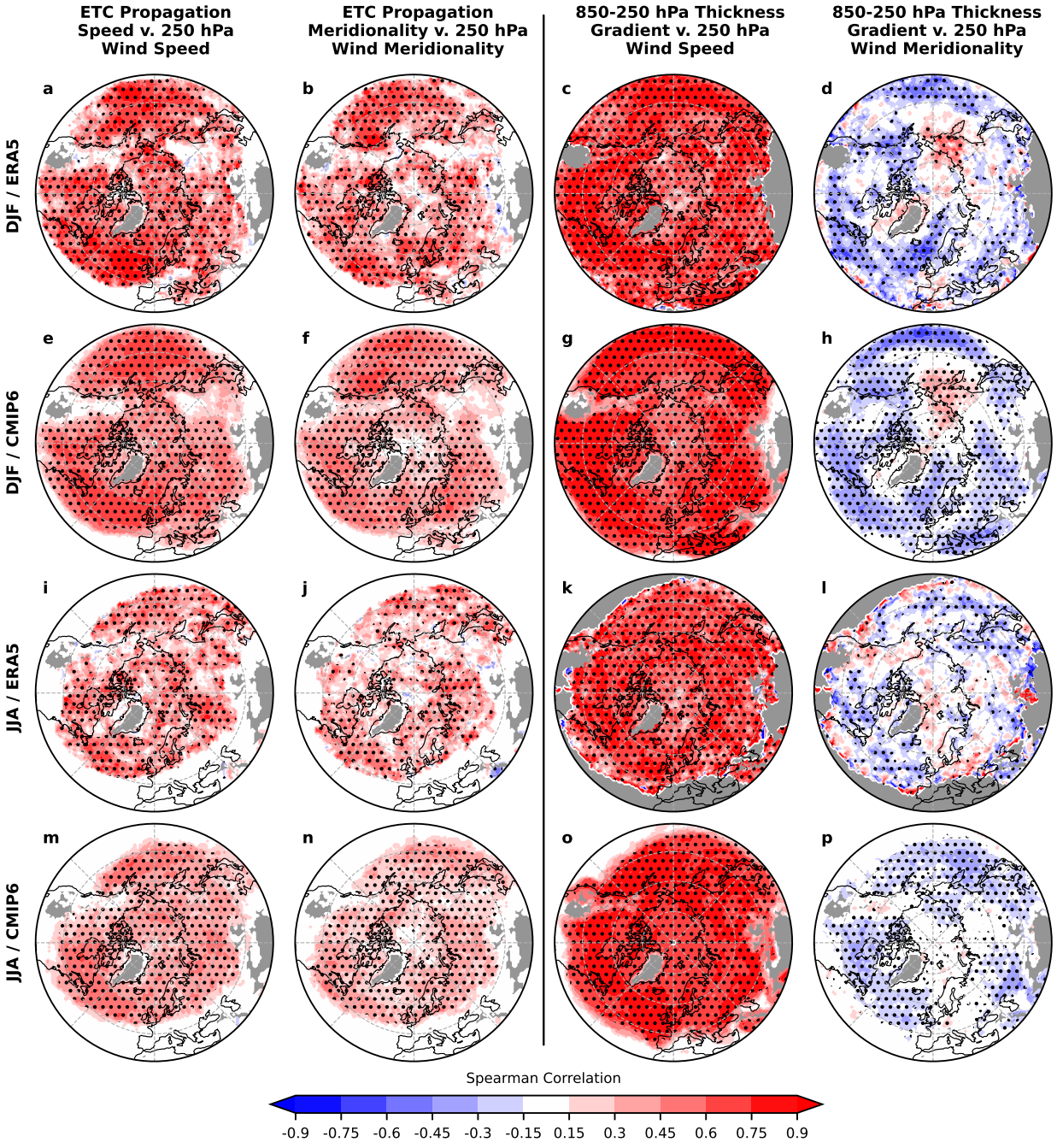

FIG. 5. Correlation between 250-hPa winds, ETC propagation, and 850–250-hPa thickness gradients during the (a)–(h) winter and (i)–(p) summer seasons. Seasonal averages (1980–2014) of (left) wind speed and (left center) meridionality within 600 km of a ETC center are correlated with the propagation speed and meridionality of ETCs. The local 850–250 thickness gradient is similarly correlated with (right center) wind speed and (right) meridionality. For ERA5 [in (a)–(d) and (i)–(l)], stippling indicates a significant correlation ($p < 0.05$). For the multimodel mean of seven high-resolution CMIP6 models [in (e)–(h) and (m)–(p)], stippling indicates that at least 80% of models agree on the sign of the correlation. Gray shading indicates no data. (Note that only seven of eight high-resolution models had daily geopotential data.)

results in weaker upper-level winds over the midlatitudes and stronger upper-level winds over the Arctic (Fig. 6d). Summer ETC propagation speed exhibits slowing throughout much of the midlatitudes (Figs. 3e/6f), which follows the change in upper-level winds. However, trends in ETC propagation speed are less robust or widespread than trends in the upper-level winds. Also, upper-level winds become faster over the Arctic, but ETC propagation speed shows no change.

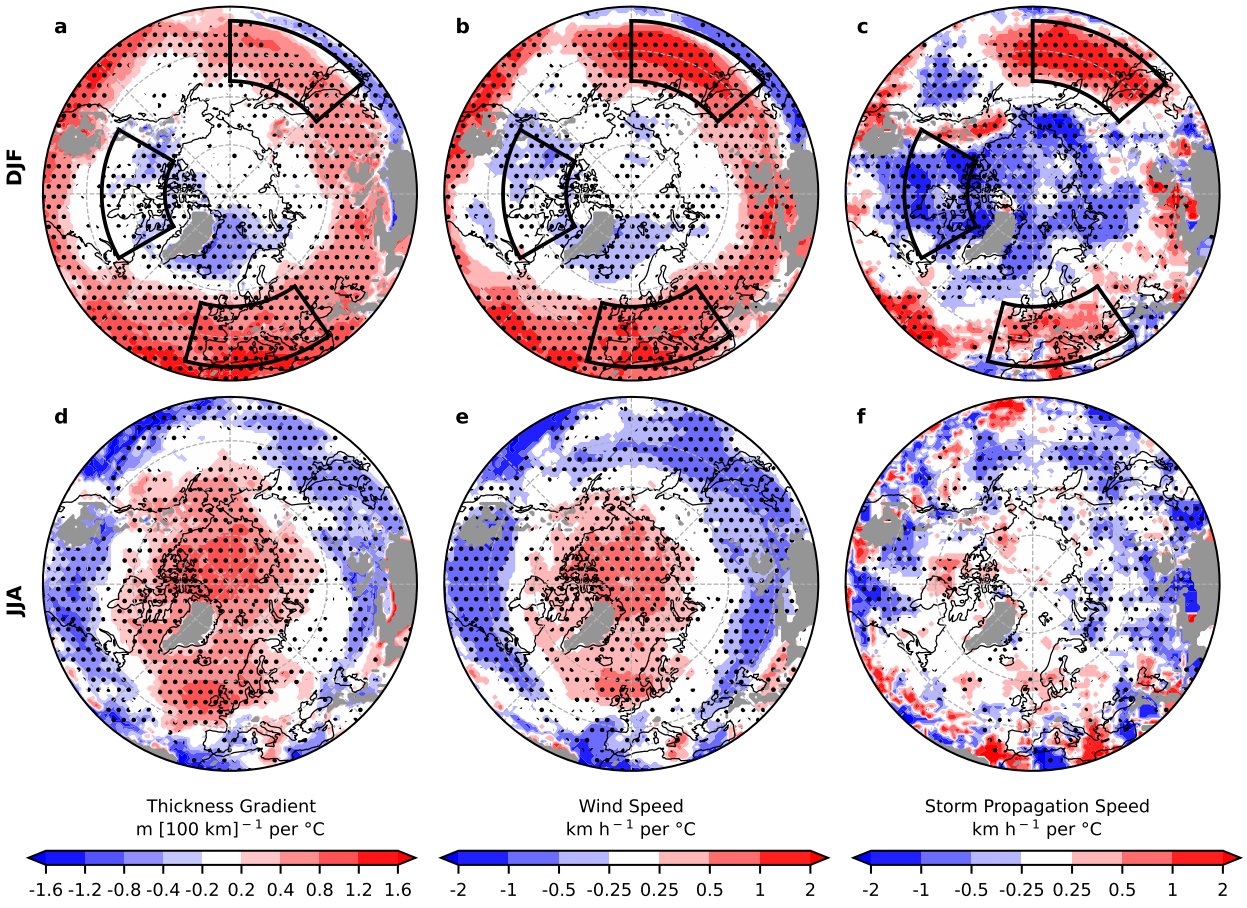

FIG. 6. Response of Northern Hemisphere (left) thickness gradients, (center) 250-hPa wind speed, and (right) storm propagation speed per 1°C warming of the average global annual temperature during (a)–(c) winter and (d)–(f) summer. Data used are from Historical+SSP5-8.5 simulations using the seven high-resolution CMIP6 models with daily geopotential data (1980–2099). Stippling indicates that at least 80% of models agree on the sign of the coefficient. Gray shading indicates no data. Black outlines in (a)–(c) show averaging regions for Fig. 7, below.

In summary, Fig. 6 shows that whether upper-level winds strengthen or weaken in response to warming is closely tied to the response of the 850–250-hPa thickness gradient, as expected from the thermal wind relationship. Additionally, Fig. 6 shows that changes to the upper-level wind regime as the world warms correspond to changes in ETC propagation, especially in the midlatitudes, and especially in winter. These connections are much weaker in summer, where model agreement for ETC propagation is poor.

2) REGIONAL THICKNESS GRADIENTS

The results presented thus far focus on the local relationship between thickness gradients, upper-level winds, and ETC propagation. However, most past literature has focused instead on regional or hemisphere-wide gradients in temperature or tropospheric thickness (e.g., Francis and Vavrus 2015; Kornhuber and Tamarin-Brodsky 2021). To demonstrate how regional and local methods compare, we examined winter ETC propagation speed in three notable regions: Canada, the western North Pacific Ocean, and central/southern Europe (Fig. 7). For each region (outlined in Fig. 6), we averaged the trend (relative to global surface temperature anomaly) of winter ETC propagation speed. We also computed the trend in the difference between average 850–250-hPa thickness in the midlatitudes (30°–60°N) and Arctic (60°–90°N) for each region's longitudinal extent.

Every model (even the low-resolution models) shows that as global warming progresses, winter ETCs move faster over the western Pacific but slower over Canada. Winter ETCs move faster over Europe for most models, but not all. This is consistent with Figs. 3b and 6c, where the western Pacific and Canada show strong model agreement but Europe does not. The results for Europe and the western Pacific demonstrate that the more the regional polar/midlatitude thickness difference increases in a model, the more ETC propagation speed increases. This aligns with the results in Fig. 5. However, no significant relationship exists for Canada in winter or for any of these regions in summer (Fig. S9 in the online

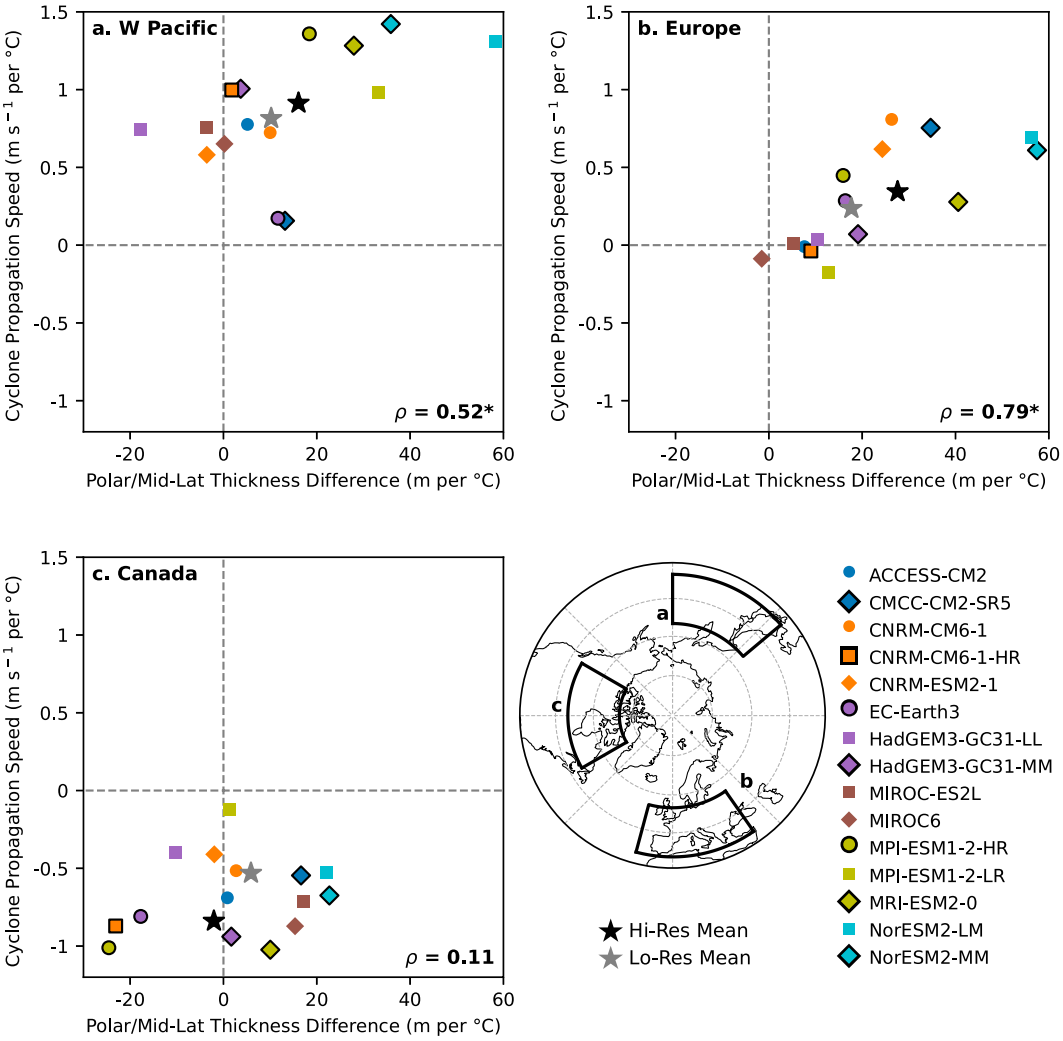

FIG. 7. Comparison of regional winter ETC propagation speed and regional thickness gradient trends. The trend in winter ETC propagation speed (relative to global annual temperature anomaly 1980–2099) from Fig. 6c is averaged (y axis) for three regions: (a) the western North Pacific (35°–55°N, 130°E–180°), (b) Europe (35°–55°N, 15°W–35°E), and (c) Canada (50°–70°N, 120°–60°W). The difference in average 850–250-hPa thickness between the midlatitudes (30°–60°N) and Arctic (60°–90°N) is calculated for each longitude range, and its trend is plotted on the x axis. Spearman's correlation is noted in the lower right of each plot, with an asterisk if significant ($p < 0.05$).

supplemental material), in contrast to past work (Kornhuber and Tamarin-Brodsky 2021).

For the western Pacific and Europe, most or all models project a strengthening of both regional and local thickness gradients (Figs. 7a,b and 6a). However, the results for Canada are inconsistent. The regional thickness gradients indicate that there is no clear change, but looking locally, it becomes evident that the thickness gradients strengthen south of about 40°N and weaken north of about 55°N in at least seven of eight high-resolution models (Fig. 6a). Taking the difference in 850–250-hPa thickness between the midlatitudes and Arctic obscures this spatial variability. In other words, the local metrics provide greater detail for how ETCs, upper-level winds, and the tropospheric thickness gradient interact.

e. *Controls on the meridionality of ETC propagation*

Environmental controls on the meridionality of ETC propagation are less straightforward than the controls on ETC propagation speed, so we examine three interrelated metrics to obtain a more holistic understanding: the local upper-level winds, local blocking, and the sinuosity of regional midtropospheric flow. Upper-level wind characteristics and sinuosity of flow describe the average state of environmental conditions. Blocking, by contrast, is a discrete event.

1) LOCAL UPPER-LEVEL WIND

Whereas the patterns for trends in upper-level wind speed are distinguished by latitude, the patterns for trends in wind meridionality are distinguished by longitude (Figs. 8c,g). In

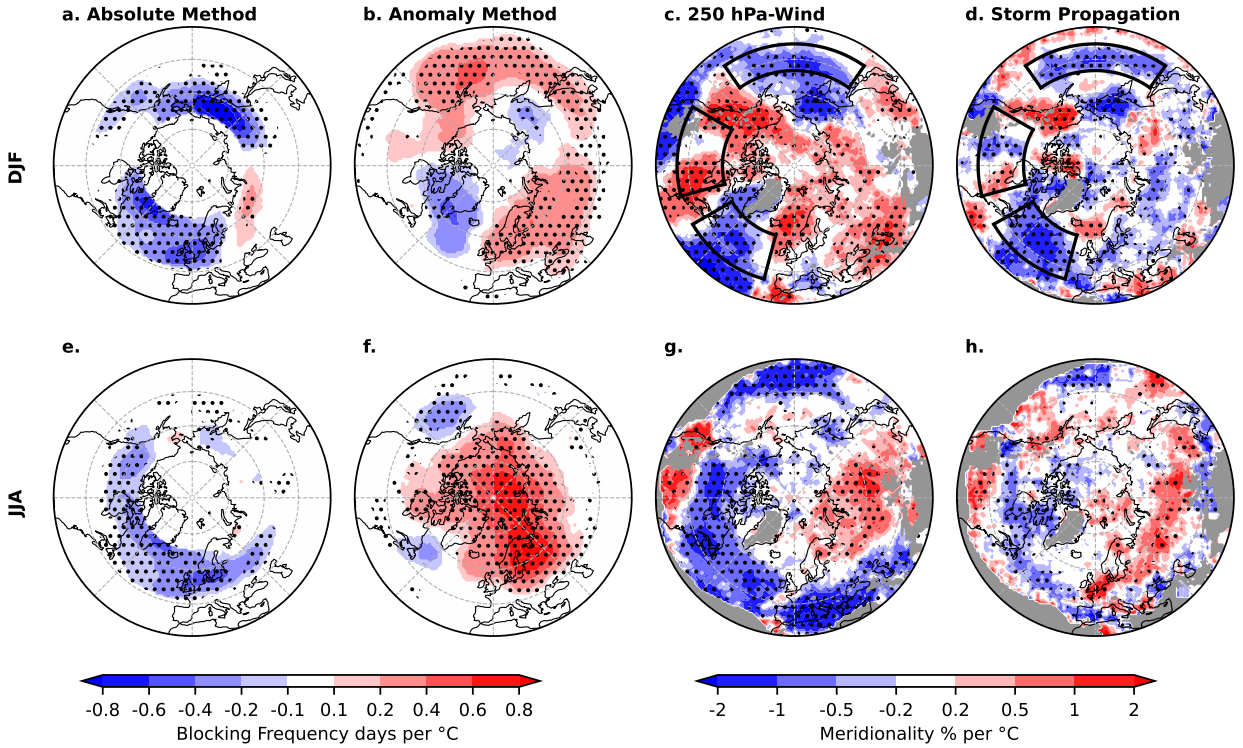

FIG. 8. Response of Northern Hemisphere (a),(b),(e),(f) blocking; (c),(g) 250-hPa wind meridionality; and (d),(h) storm propagation meridionality per 1°C warming of the average global annual temperature during (top) winter and (bottom) summer. Data used are from Historical+SSP5-8.5 simulations using the seven high-resolution CMIP6 models with daily geopotential data (1980–2099). Stippling indicates that at least 80% of models agree on the sign of the coefficient. Gray shading indicates no data. Black outlines in (c) and (d) show averaging regions for Fig. 9, below.

winter, upper-level winds become more meridional (red shading) over North America and the Nordic seas but more zonal (blue shading) over much of the Pacific and Atlantic Oceans. This aligns with the changes to 300-hPa meridional winds under SSP5-8.5 reported by Simpson et al. (2021; see their Fig. 6g). In summer, upper-level winds become more meridional over central Eurasia and generally more zonal elsewhere.

Trends in meridionality of upper-level winds correspond to trends in meridionality of ETC propagation in winter for most of the Northern Hemisphere, but not 45°–100°E over Eurasia (Fig. 8c vs Fig. 8d). In summer, almost every area with a robust trend in ETC propagation meridionality corresponds to a robust trend in upper-level wind meridionality; however, robust trends are less widespread for ETC propagation meridionality than for upper-level wind meridionality. In other words, the correspondence between meridionality of upper-level winds and ETC propagation is not as strong as the correspondence between speed of upper-level winds and ETC propagation.

2) BLOCKING FREQUENCY

ETC propagation can also be affected by intermittent events, such as atmospheric blocking (Davini et al. 2012; Booth et al. 2017). More specifically, the propagation direction of ETCs can become more meridional when blocking is more prevalent. For example, blocking over the Gulf of Alaska helps steer ETCs poleward into the Bering Strait (Mesquita et al. 2009; Crawford et al. 2020), and blocking over Greenland helps steer ETCs poleward into Baffin Bay (Serreze et al. 2022). One may hypothesize, then, that the trends toward more-zonal propagation that dominate the winter are related to less-frequent blocking.

To test this, we applied two blocking identification methods (described in section 2c). The absolute method tends to highlight disruptions or shifts in the jet stream and poleward excursions of subtropical air; whereas the anomaly method highlights anticyclonic areas within the main storm tracks (Schwierz et al. 2004; Woollings et al. 2018). As such, it is unsurprising that trends in blocking based on the absolute method closely follow trends in the meridionality of the 250-hPa wind, but the trends in blocking based on the anomaly method do not (Fig. 8).

Using the absolute method, broad areas of decreased winter blocking in response to warming over eastern Siberia and the North Atlantic (Fig. 8a) correspond to areas of decreased meridionality in upper-level winds and ETCs (Figs. 8c,d). In summer, the broad area of decreased blocking extending from North America to western Eurasia from 45° to 60°N also corresponds to decreased meridionality in upper-level winds, but ETCs show decreased meridionality over a narrower

latitudinal band and only over North America and the North Atlantic (Figs. 8e,g,h). There are also some areas (e.g., eastern North America or the Norwegian Sea in winter) that exhibit more-meridional flow in 250-hPa winds despite a decline in blocking. The discrepancy between absolute blocking and the meridionality of 250-hPa winds is counterintuitive at first, but 250-hPa winds are not perfectly zonal in the absence of blocking, and a blocking event is only identified if certain intensity, size, and duration thresholds are met. It is entirely possible, then, for winds to become more meridional in their mean state even as variability large enough to constitute punctuated blocking events is reduced.

Using the anomaly method yields vastly different results. Most areas that showed negative blocking trends in the absolute method show no trend in the anomaly method (Figs. 8a,e vs Figs. 8b,f). Instead, many regions exhibit positive trends in blocking in response to warming, and these do not consistently correspond to trends in meridionality of either upper-level winds or ETCs. Additionally, neither blocking metric helps explain why ETC propagation becomes more zonal over western Siberia despite more-meridional 250-hPa winds.

Several prior studies also used an absolute blocking index to assess future trends, and each one found an overall decline in blocking under future warming scenarios (Masato et al. 2013; Matsueda and Endo 2017; Woollings et al. 2018; Davini and D'Andrea 2020). Use of the anomaly index is less common, but results derived from Woollings et al. (2018) using the same anomaly method agree with ours. Most notably, they also find increased blocking over Europe, the Arctic Ocean, and the Pacific storm track in winter. Besides disagreement between different metrics, another limitation of our blocking analysis is that blocking events are generally underestimated by CMIP6 models (Schiemann et al. 2020). Correcting for bias in the mean state of geopotential height can greatly reduce bias in absolute blocking (Scaife et al. 2010), so one might expect the anomaly method (which is not dependent on the mean state) to better match observations. However, Schiemann et al. (2020) showed this was not the case for CMIP6 models. Therefore, blocking trends and their relationship to ETC propagation merit further investigation. Those caveats in mind, we can say that 1) trends using the absolute method provide the better match to trends in meridionality of ETC propagation, and 2) decreased blocking over the Atlantic and eastern Siberia in winter align with more-zonal ETC propagation.

3) Sinuosity of midtropospheric flow

We also analyze the sinuosity of the average 500-hPa isohypse [following Cattiaux et al. (2016)], which provides a regional or hemispherical measure of waviness in midtropospheric flow. (For an instantaneous example, see Fig. S10 in the online supplemental material.) Higher sinuosity means either a higher wavenumber or greater wave amplitude, but in either case the flow is likely to be more meridional. Therefore, it is logical that over both the North Atlantic and North Pacific Oceans, where ETC propagation becomes more zonal in winter in response to warming, the 500-hPa flow also becomes less sinuous for nearly every model (Fig. 9). Over North America, trends in both 500-hPa sinuosity and the meridionality of ETC propagation were more mixed, with less model agreement (Fig. 9b). Note, though, that trends over North America for sinuosity and ETC meridionality have a significant positive correlation, meaning that the models with more positive trends in sinuosity also tend to exhibit more positive trends in the meridionality of ETC propagation. This suggests that model disagreement for the trend in ETC meridionality is related to the disagreement for the trend in sinuosity. Interestingly, North America is the only region of the three exhibiting a significant statistical link. Model variation in the meridionality of ETC propagation is even more closely tied to sinuosity at 500 hPa in summer (Fig. 10)—with significant correlations exhibited in all three regions. Models disagree on the sign of the trends for North America (Fig. 10b), but nearly all simulate more-zonal propagation within the oceanic storm tracks occurring in concert with less-sinuous midtropospheric flow.

Combining the findings from these three metrics (local upper-level winds, blocking, and the sinuosity of regional midtropospheric flow), we can conclude that increasingly zonal propagation of ETCs in the Pacific storm track in winter and the Atlantic storm track in both seasons is closely related to less-sinuous and increasingly zonal mid/upper-level flow. Using the absolute method, these patterns are also associated with decreased blocking. The future of ETC propagation over the continents is less certain, in part because there is less model agreement about how these top-down influences will respond to warming. Trends in the meridionality of upper-level winds are the best match to trends in the meridionality of ETCs in winter. In summer, when upper-level winds are weaker, the meridionality of ETCs is most strongly linked the sinuosity of midlevel flow.

4) Regional thickness differences

Last, we compare the trends in winter ETC meridionality of three key regions with the trends in the winter polar/midlatitude thickness difference (Fig. 11). The strength of the regional thickness gradient is negatively correlated with sinuosity of 500-hPa flow (Fig. S11 in the online supplemental material), meaning that a stronger thickness gradient translates to less wavy 500-hPa flow. Accordingly, there is a negative correlation between the trend a model exhibits for the polar/midlatitude thickness difference and the trend it exhibits for ETC propagation meridionality over North America. The thickness gradient also strengthens over the North Atlantic in almost every model, consistent with less-sinuous 500-hPa flow and more-zonal ETC propagation. However, there is no clear relationship in the North Pacific. Summer yields similar results (Fig. S12 in the online supplemental material). Therefore, although not as important to meridionality as to speed, the trends of thickness gradients found in CMIP6 models do have some implications for meridionality of ETC propagation.

4. Discussion

a. Connecting results to past studies

In these CMIP6 models, storm propagation exhibits greater sensitivity to global warming in winter than in summer, with a

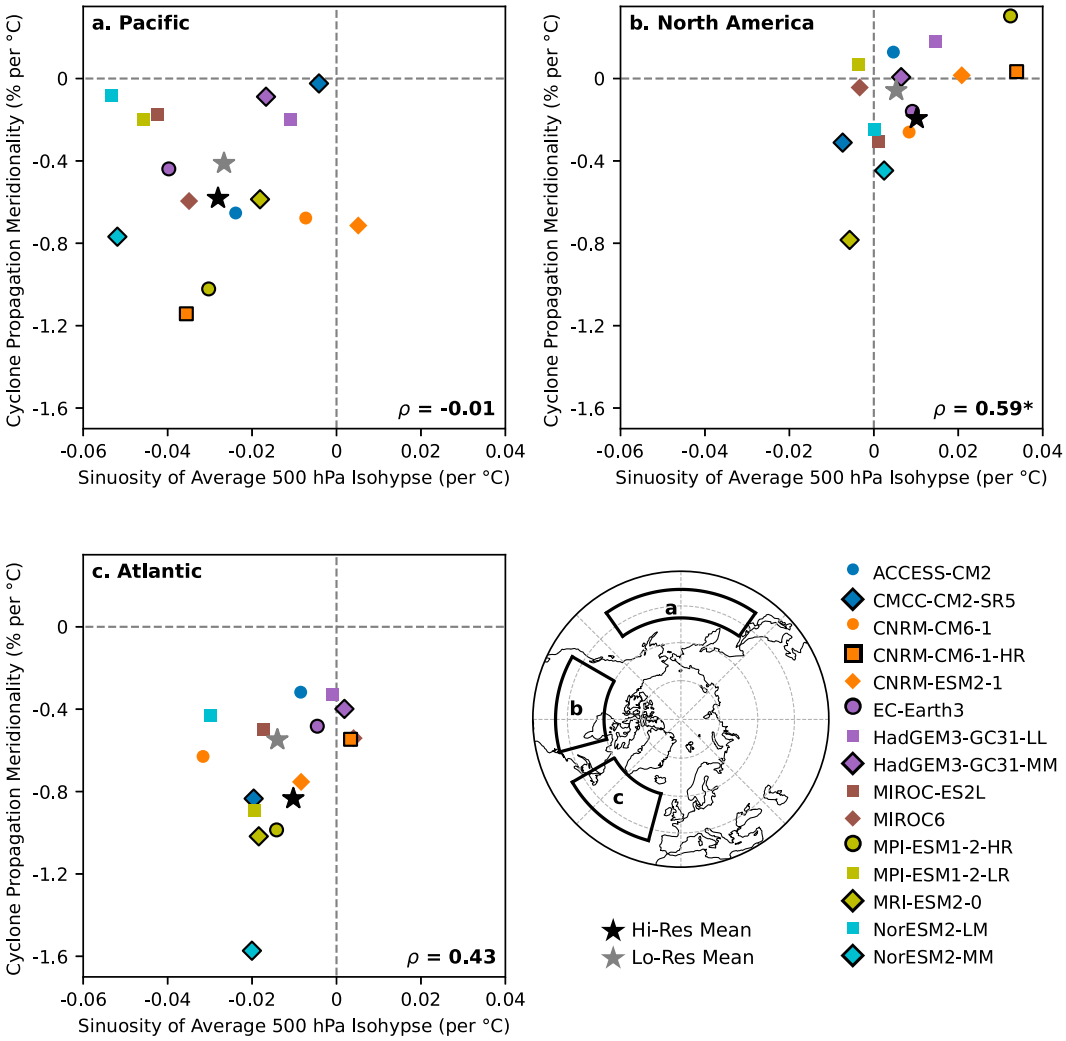

FIG. 9. Comparison of trends in regional winter ETC propagation meridionality and regional sinuosity of the 500-hPa isohypse. The trend in winter ETC propagation meridionality (relative to global annual temperature anomaly 1980–2099) from Fig. 8d is averaged (y axis) for three regions: (a) the North Pacific (38°–50°N, 145°–215°E), (b) North America (40°–60°N, 120°–75°W), and (c) the North Atlantic (40°–60°N, 60°–15°W). The average sinuosity of the average 500-hPa isohypse is calculated for each longitude range, and its trend is plotted on the x axis. Spearman's correlation is noted in the lower right of each plot, with an asterisk if significant ($p < 0.05$).

trend toward faster winter propagation in the western Pacific and parts of the Atlantic-European storm track and slower propagation over North America and the Arctic (Fig. 3). In summer, models exhibit weaker trends and less consistency than in winter, but slowing of storm propagation is likely throughout midlatitude Asia, the Pacific, and North America. Our summer results for ETC propagation speed are broadly consistent with past work emphasizing more persistent weather patterns (e.g., Francis et al. 2018; Pfleiderer et al. 2019; Kornhuber and Tamarin-Brodsky 2021), although we find stronger trends in winter.

Changes in storm propagation speed are tightly linked to changes in upper-level wind speed, which in turn are strongly linked to the local 850–250-hPa thickness gradient (Figs. 5 and 6). This connection is similar to past findings for summer weather patterns (Kornhuber and Tamarin-Brodsky 2021), although we find a stronger relationship in winter than summer. Additionally, the relationship between thickness gradients and storm propagation speed may be obscured if examining regional instead of local metrics (Fig. 7; section 4b).

To explain why storm propagation over the oceans might become more zonal, we examined top-down influences on storm propagation using three interrelated measures: the meridionality of 250-hPa winds, the frequency of blocking, and the sinuosity of the average 500-hPa isohypse. None of these measures provide a perfect match to ETC propagation, but together they show that areas where ETC propagation becomes more zonal tend to connect to a related set of changes to mid- and upper-level flow: more-zonal 250-hPa winds, less sinuosity at the 500-hPa level, and/or less blocking. The

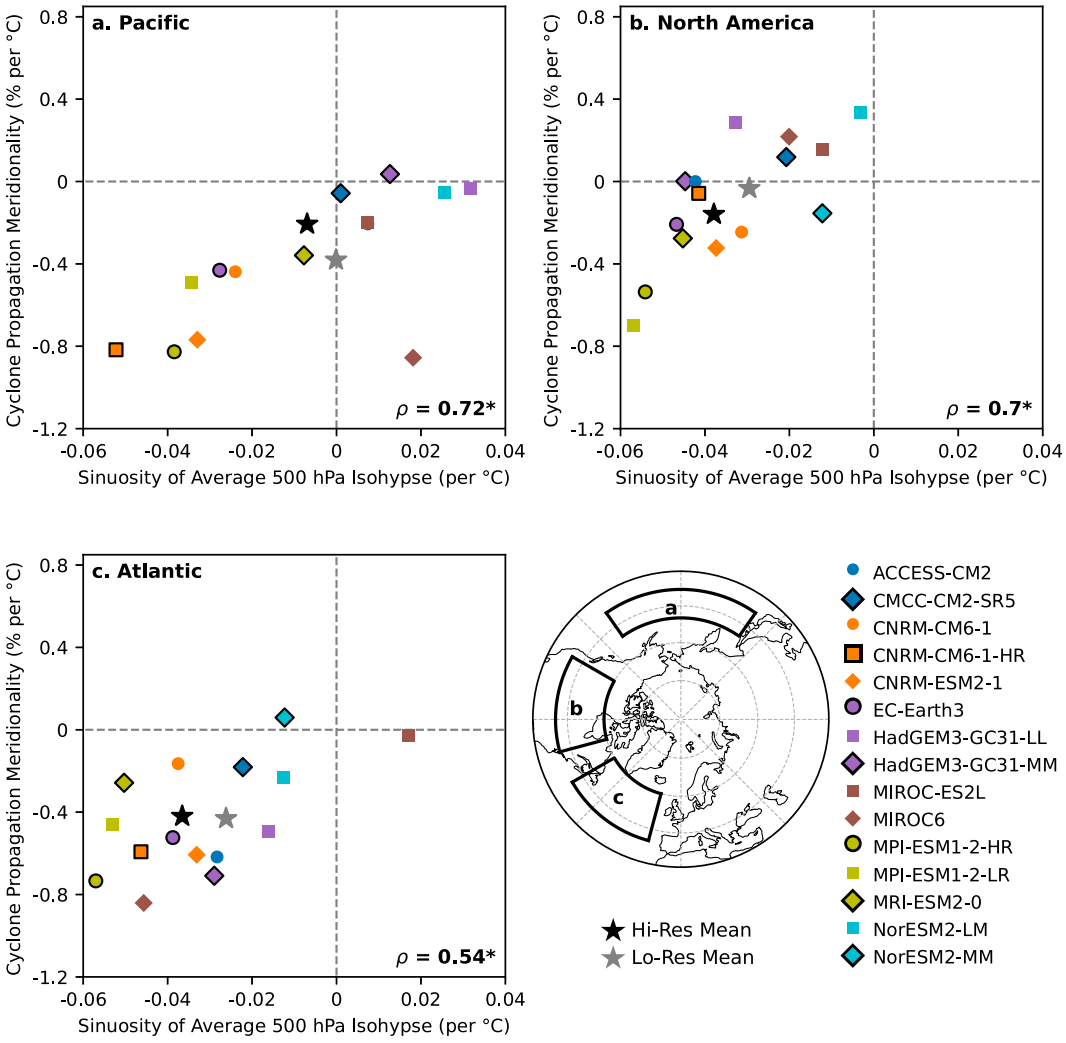

FIG. 10. As in Fig. 9, but for summer.

relationship we find between tropospheric thickness gradients and both 500-hPa sinuosity and the meridionality of upper-level winds is consistent with the negative correlation between low-level meridional temperature gradients and the amplitude of stationary waves (Wills et al. 2019).

The increased zonality of storm propagation in this study stands in contrast to Tamarin-Brodsky and Kaspi (2017). Increased poleward displacement of storms in that study was connected to the bottom-up influence of enhanced latent heating as the Atlantic warms (Held and Soden 2006; Tamarin and Kaspi 2017). At least in the CMIP6 models used here, the top-down influences of large-scale circulation may overcome enhanced latent heating from a warming ocean. A more targeted comparison of CMIP5 and CMIP6 would be needed to confirm this. Closer examination of how diabatic heating in ETCs is represented in CMIP6 models may also reveal physical reasons for some of the exceptions to the general patterns we observed (e.g., why winter storms over central Eurasia become more zonal with warming even though the upper-level winds become more meridional).

b. *Limitations*

One limitation of this study is the small number of models used. Only 18 CMIP6 models had sufficient data (6-h SLP fields for both Historical and SSP5-8.5 experiments). Of those, only eight had nominal resolutions of 100 km or finer, and only seven of those included (sub)daily thickness fields. This creates an ensemble that may be sensitive to individual model bias or internal variability. Additionally, using linear regression to summarize sensitivity of ETC characteristics to global temperature obscures any nonlinear changes. However, using discrete differencing instead of linear regression reveals the same spatial patterns of positive and negative tendencies in response to warming (Figs. S13–S15 in the online supplemental material).

Another limitation is that the magnitude of bias between even high-resolution models and ERA5 (Figs. 1 and 2) is

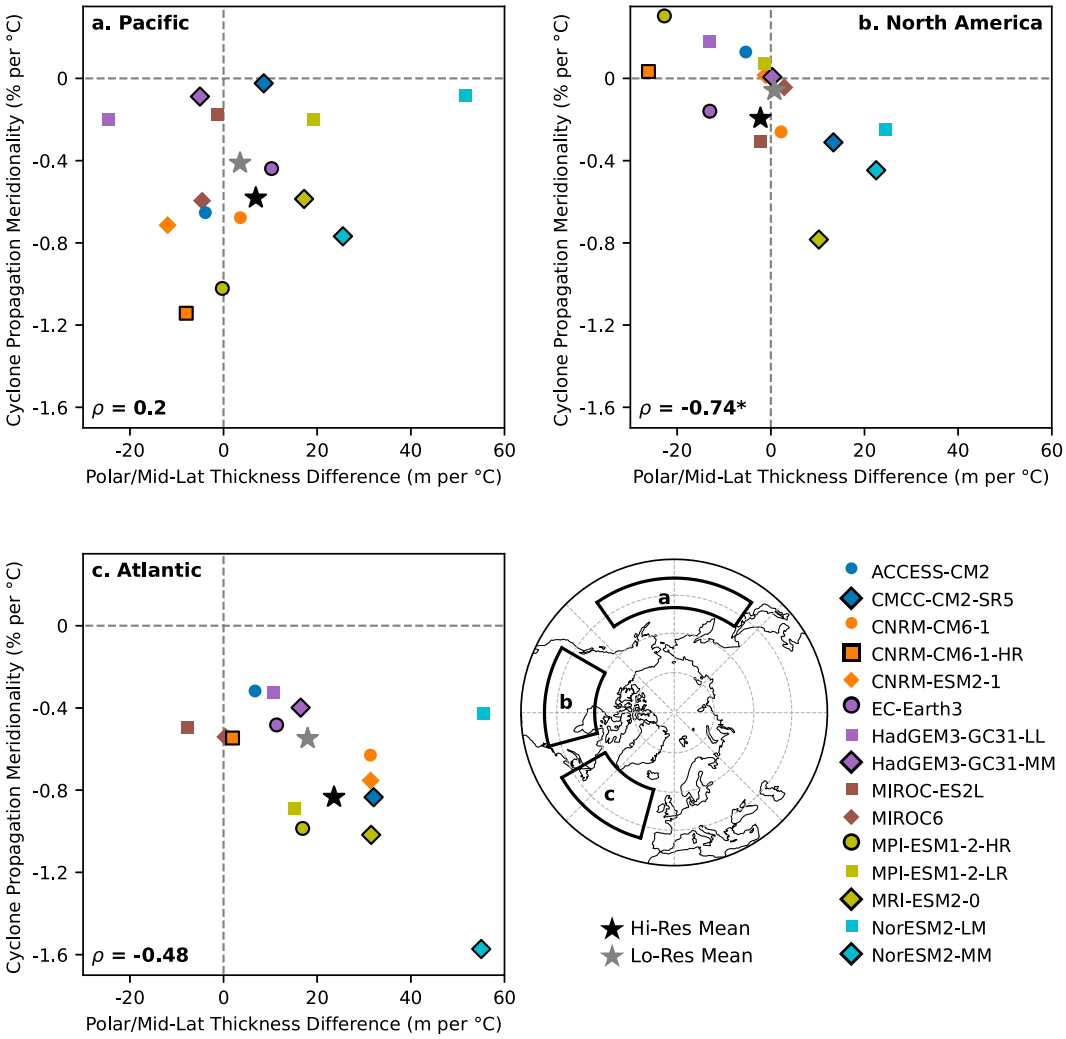

FIG. 11. Comparison of regional winter ETC propagation meridionality and regional thickness gradient trends. The trend in winter ETC propagation meridionality (relative to global annual temperature anomaly 1980–2099) from Fig. 8d is averaged (y axis) for three regions: (a) The North Pacific (38°–50°N, 145°–215°E), (b) North America (40°–60°N, 120°–75°W), and (c) the North Atlantic (40°–60°N, 60°–15°W). The difference in average 850–250-hPa thickness between the midlatitudes (30°–60°N) and Arctic (60°–90°N) is calculated for each longitude range, and its trend is plotted on the x axis. Spearman's correlation is noted in the lower left of each plot, with an asterisk if significant ($p < 0.05$).

often greater than the amount of change in ETC characteristics for 1°C of global warming (Fig. 3). With a temperature anomaly of 4°C (i.e., 3°C warmer than present day), the change to ETC propagation exceeds the bias in winter, but generally not in summer (Fig. S15 in the online supplemental material vs Fig. 2). Therefore, projected changes to ETC propagation in winter are more likely to be meaningful.

CMIP6 models are known to overestimate warming during the historical period, especially in summer (McKitrick and Christy 2020; Tokarska et al. 2020; Fig. 12, left). This bias is controlled for by calculating all future projections relative to the amount of annual global warming (instead of time). In addition, limiting analysis to only those models with reasonable estimates of historical global warming and Arctic amplification (i.e., models within the red box in Fig. 12a) does not change the results (Fig. S16 vs Fig. S17 in the online supplemental material).

Potential bias also exists in the horizontal and vertical distribution of warming (Fig. S18 in the online supplemental material), with implications for local (Fig. 6) and regional (Figs. 7 and 11; Francis and Vavrus 2015; Ye and Messori 2021) thickness gradients, as well as the broader investigation of the impacts of Arctic amplification on midlatitude weather (Smith et al. 2019; Cohen et al. 2020; Blackport and Screen 2020). For example, CMIP6 models tend to overestimate historical upper-tropospheric warming in the lower latitudes (McKitrick and Christy 2020; Keil et al. 2021) while underestimating upper-tropospheric warming in the Arctic (He et al. 2020;

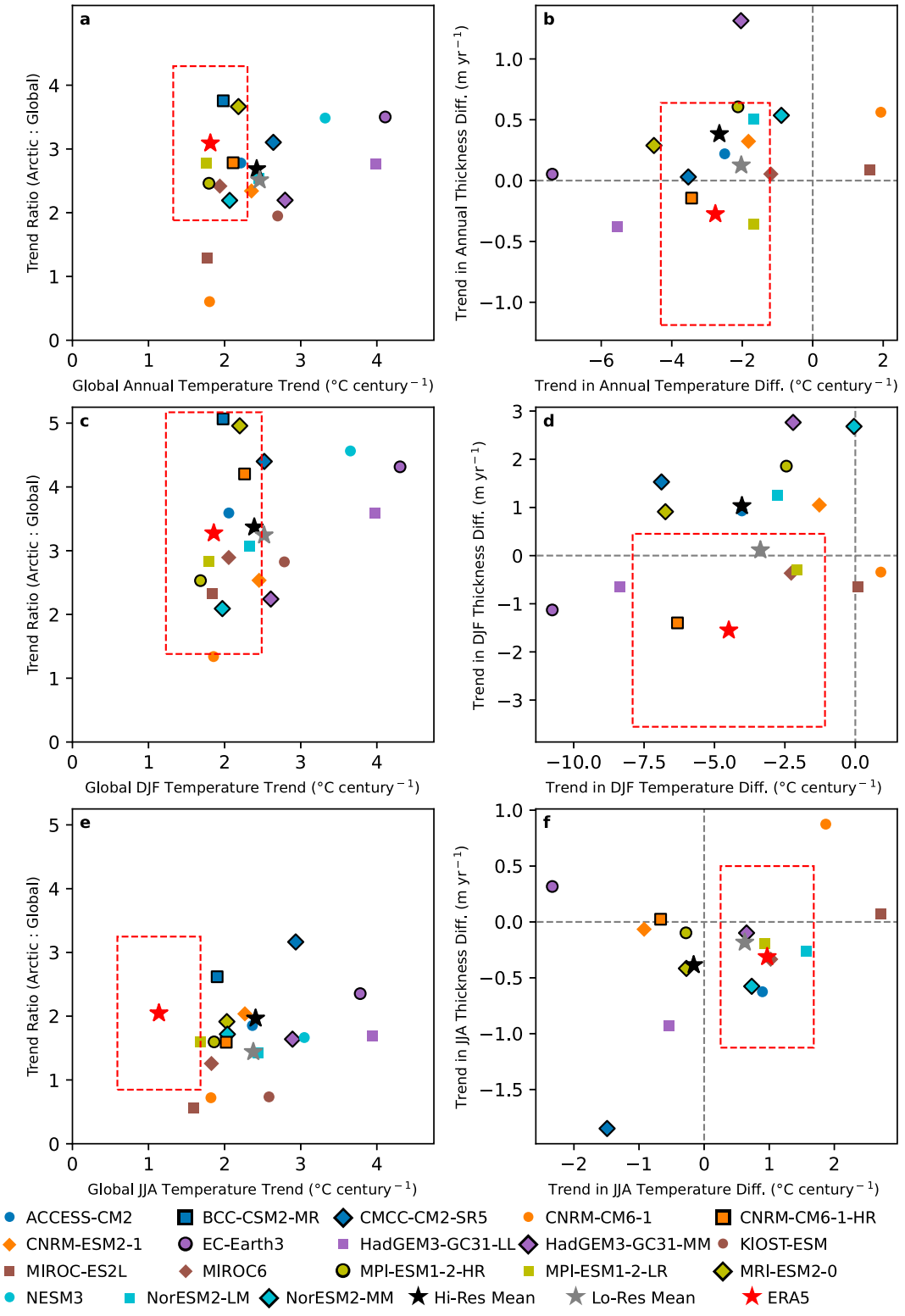

FIG. 12. Global warming and Arctic amplification in CMIP6 models: (left) Arctic amplification of global warming is measured as the ratio of the Arctic (60°–90°N) vs global annual 2-m temperature trends for the period 1980–2014. (right) Trend in the difference between Arctic and midlatitudes (30°–60°N) 2-m temperature and 850–250-hPa thickness. Symbols with black edges represent high-resolution models. The black and gray stars are the multimodel means of those first simulations for high- and low-resolution models, respectively. The red-outlined box indicates the 95% confidence interval for the ERA5 trends or trend ratios.

Ye and Messori 2021). This impacts how CMIP6 models portray both local and hemisphere-wide gradients in tropospheric thickness. For example, with midlatitude North America warming slower than either the Arctic or tropics, local thickness gradients strengthen across the southern United States in winter but weaken over Canada (Fig. 6a). At a larger scale, the hemisphere-wide thickness difference between midlatitudes and the Arctic weakened for the period 1980–2014 based on ERA5 data, but that difference increased for most CMIP6 models (Fig. 12, right, *y* axis). In winter (Fig. 12d), the high-resolution multimodel mean is also beyond the 95% confidence interval for ERA5; however, the ERA5 trend is not statistically significant and the sign of the CMIP6 trends is not consistently positive.

There is also substantial evidence that historical discrepancies between upper-level warming rates in observations versus climate models are largely explainable by internal variability of poleward heat transport (Perlwitz et al. 2015; He et al. 2020; Po-Chedley et al. 2021; Ye and Messori 2021). Indeed, when analyses are extended beyond 1980–2014 to include more recent years, observed relations between Arctic sea ice loss and atmospheric circulation weaken (Blackport and Screen 2020; Smith et al. 2022), coming closer to model results. Therefore, the CMIP6 multimodel mean trend in thickness gradients may be a realistic representation of the forced response to long-term global warming despite differences with ERA5. Additional analyses through efforts like the Polar Amplification Model Intercomparison Project (Smith et al. 2019, 2022) will continue to refine our understanding.

5. Conclusions

The results reported here enhance our understanding of ETC propagation in a warming world in several ways. We showed that models with a higher spatial resolution (100-km nominal resolution or finer) outperform coarser models at matching observed ETC propagation speed and meridionality, although they still exhibit some regional biases. Using these higher-resolution models, projections of ETC propagation are regionally and seasonally variable. In winter, slower ETC propagation throughout North America and poleward of 60°N contrasts with faster propagation in the Pacific. ETC propagation also becomes more zonal. In summer, trends are weaker, although trends toward slower propagation are most common. Propagation becomes more zonal over Canada and part of the North Atlantic but more meridional over parts of Eurasia.

These trends were then related to various metrics that describe top-down steering by mid- and upper-level tropospheric flow. Trends in ETC propagation speed can mostly be explained by changes in the 250-hPa wind, which in turn is controlled by trends in local 850–250-hPa thickness gradients. Possible controls on meridionality showed weaker relationships, but in general, the places experiencing more-zonal ETC propagation could be linked to at least one of three factors: more-zonal 250-hPa winds, lower sinuosity of 500-hPa flow, and/or decreased blocking. In some regions, these trends also connect back to the trends in 850–250-hPa thickness gradients.

Our findings for ETC propagation speed were generally consistent with past work, but our results showing more-zonal propagation over the main oceanic storm tracks in the future contradict past findings, which emphasized the impact of latent heating on latitudinal displacement of storms. By linking our results to mid- and upper-level circulation, we suggest that these large-scale, top-down influences may be outweighing bottom-up influences, like latent heating, in CMIP6 models. How realistic this projection is depends on how well models project trends in diabatic heating in ETCs, mid- and upper-level flow, and even the large-scale balance of heating in the midlatitudes versus the Arctic.

Acknowledgments. This work is supported by the Canada Research Chairs Program 150 and the Natural Sciences and Engineering Research Council of Canada RGPIN-2020-05689.

Data availability statement. CMIP6 data were downloaded from the Earth System Grid Federation (https://esgf-node.llnl.gov/search/cmip6/) using code from Thiago Loureiro (https://doi.org/10.5281/zenodo.3966555). ERA5 data were downloaded from Copernicus Climate Change Service (https://doi.org/10.24381/cds.bd0915c6, https://doi.org/10.24381/cds.adbb2d47, and https://doi.org/10.24381/cds.f17050d7). Cyclone detection and tracking code is available online (https://doi.org/10.5281/zenodo.4356161).

REFERENCES

Akperov, M., and Coauthors, 2019: Future projections of cyclone activity in the Arctic for the 21st century from regional climate models (Arctic-CORDEX). *Global Planet. Change*, **182**, 103005, https://doi.org/10.1016/j.gloplacha.2019.103005.

Blackport, R., and J. A. Screen, 2020: Insignificant effect of Arctic amplification on the amplitude of midlatitude atmospheric waves. *Sci. Adv.*, **6**, eaay2880, https://doi.org/10.1126/sciadv.aay2880.

Booth, J. F., E. Dunn-Sigouin, and S. Pfahl, 2017: The relationship between extratropical cyclone steering and blocking along the North American East Coast. *Geophys. Res. Lett.*, **44**, 11 976–11 984, https://doi.org/10.1002/2017GL075941.

Cattiaux, J., Y. Peings, D. Saint-Martin, N. Trou-Kechout, and S. J. Vavrus, 2016: Sinuosity of midlatitude atmospheric flow in a warming world. *Geophys. Res. Lett.*, **43**, 8259–8268, https://doi.org/10.1002/2016GL070309.

Chan, K. T. F., 2019: Are global tropical cyclones moving slower in a warming climate? *Environ. Res. Lett.*, **14**, 104015, https://doi.org/10.1088/1748-9326/ab4031.

Chang, E. K. M., 2013: CMIP5 projection of significant reduction in extratropical cyclone activity over North America. *J. Climate*, **26**, 9903–9922, https://doi.org/10.1175/JCLI-D-13-00209.1.

Cohen, J., and Coauthors, 2020: Divergent consensuses on Arctic amplification influence on midlatitude severe winter weather. *Nat. Climate Change*, **10**, 20–29, https://doi.org/10.1038/s41558-019-0662-y.

Crawford, A. D., and M. C. Serreze, 2016: Does the summer Arctic frontal zone influence Arctic Ocean cyclone activity? *J. Climate*, **29**, 4977–4993, https://doi.org/10.1175/JCLI-D-15-0755.1.

——, and ——, 2017: Projected changes in the Arctic frontal zone and summer Arctic cyclone activity in the CESM Large Ensemble. *J. Climate*, **30**, 9847–9869, https://doi.org/10.1175/JCLI-D-17-0296.1.

——, K. E. Alley, A. M. Cooke, and M. C. Serreze, 2020: Synoptic climatology of rain-on-snow events in Alaska. *Mon. Wea. Rev.*, **148**, 1275–1295, https://doi.org/10.1175/MWR-D-19-0311.1.

——, E. A. P. Schreiber, N. Sommer, M. C. Serreze, J. C. Stroeve, and D. G. Barber, 2021: Sensitivity of Northern Hemisphere cyclone detection and tracking results to fine spatial and temporal resolution using ERA5. *Mon. Wea. Rev.*, **149**, 2581–2598, https://doi.org/10.1175/MWR-D-20-0417.1.

Davini, P., and F. D'Andrea, 2020: From CMIP3 to CMIP6: Northern Hemisphere atmospheric blocking simulation in present and future climate. *J. Climate*, **33**, 10021–10038, https://doi.org/10.1175/JCLI-D-19-0862.1.

——, C. Cagnazzo, S. Gualdi, and A. Navarra, 2012: Bidimensional diagnostics, variability, and trends of Northern Hemisphere blocking. *J. Climate*, **25**, 6496–6509, https://doi.org/10.1175/JCLI-D-12-00032.1.

Eichler, T. P., 2020: The impacts of a warming climate on winter mid-latitude cyclones in the NARCCAP model suite. *Climate Dyn.*, **54**, 4379–4398, https://doi.org/10.1007/s00382-020-05236-z.

——, N. Gaggini, and Z. Pan, 2013: Impacts of global warming on Northern Hemisphere winter storm tracks in the CMIP5 model suite. *J. Geophys. Res. Atmos.*, **118**, 3919–3932, https://doi.org/10.1002/jgrd.50286.

Eyring, V., S. Bony, G. A. Meehl, C. A. Senior, B. Stevens, R. J. Stouffer, and K. E. Taylor, 2016: Overview of the Coupled Model Intercomparison Project Phase 6 (CMIP6) experimental design and organization. *Geosci. Model Dev.*, **9**, 1937–1958, https://doi.org/10.5194/gmd-9-1937-2016.

Francis, J. A., and S. J. Vavrus, 2012: Evidence linking Arctic amplification to extreme weather in mid-latitudes. *Geophys. Res. Lett.*, **39**, L06801, https://doi.org/10.1029/2012GL051000.

——, and ——, 2015: Evidence for a wavier jet stream in response to rapid Arctic warming. *Environ. Res. Lett.*, **10**, 014005, https://doi.org/10.1088/1748-9326/10/1/014005.

——, N. Skific, and S. J. Vavrus, 2018: North American weather regimes are becoming more persistent: Is Arctic amplification a factor? *Geophys. Res. Lett.*, **45**, 11414–11422, https://doi.org/10.1029/2018GL080252.

——, ——, and ——, 2020: Increased persistence of large-scale circulation regimes over Asia in the era of amplified Arctic warming, past and future. *Sci. Rep.*, **10**, 14953, https://doi.org/10.1038/s41598-020-71945-4.

Hahn, L. C., K. C. Armour, M. D. Zelinka, C. M. Bitz, and A. Donohoe, 2021: Contributions to polar amplification in CMIP5 and CMIP6 models. *Front. Earth Sci.*, **9**, 710036, https://doi.org/10.3389/feart.2021.710036.

Harvey, B. J., P. Cook, L. C. Shaffrey, and R. Schiemann, 2020: The response of the Northern Hemisphere storm tracks and jet streams to climate change in the CMIP3, CMIP5, and CMIP6 climate models. *J. Geophys. Res. Atmos.*, **125**, e2020JD032701, https://doi.org/10.1029/2020JD032701.

He, S., X. Xu, T. Furevik, and Y. Gao, 2020: Eurasian cooling linked to the vertical distribution of Arctic warming. *Geophys. Res. Lett.*, **47**, e2020GL087212, https://doi.org/10.1029/2020GL087212.

Held, I. M., and B. J. Soden, 2006: Robust responses of the hydrological cycle to global warming. *J. Climate*, **19**, 5686–5699, https://doi.org/10.1175/JCLI3990.1.

Hersbach, H., and Coauthors, 2018: ERA5 hourly data on pressure levels from 1979 to present. Copernicus Climate Change Service (C3S) Climate Data Store (CDS), accessed 21 November 2021, https://doi.org/10.24381/cds.bd0915c6.

——, and Coauthors, 2020: The ERA5 global reanalysis. *Quart. J. Roy. Meteor. Soc.*, **146**, 1999–2049, https://doi.org/10.1002/qj.3803.

Hewson, T. D., and U. Neu, 2015: Cyclones, windstorms and the IMILAST project. *Tellus*, **67A** (1), 473, https://doi.org/10.3402/tellusa.v67.27128.

Huguenin, M. F., E. M. Fischer, S. Kotlarski, S. C. Scherrer, C. Schwierz, and R. Knutti, 2020: Lack of change in the projected frequency and persistence of atmospheric circulation types over Central Europe. *Geophys. Res. Lett.*, **47**, e2019GL086132, https://doi.org/10.1029/2019GL086132.

IPCC, 2021: Summary for policymakers. *Climate Change 2021: The Physical Science Basis*, V. Masson-Delmotte et al., Eds., Cambridge University Press, 3–32.

Keeley, S. P. E., R. T. Sutton, and L. C. Shaffrey, 2012: The impact of North Atlantic sea surface temperature errors on the simulation of North Atlantic European region climate. *Quart. J. Roy. Meteor. Soc.*, **138**, 1774–1783, https://doi.org/10.1002/qj.1912.

Keil, P., H. Schmidt, B. Stevens, and J. Bao, 2021: Variations of tropical lapse rates in climate models and their implications for upper tropospheric warming. *J. Climate*, **34**, 9747–9761, https://doi.org/10.1175/JCLI-D-21-0196.1.

Kornhuber, K., and T. Tamarin-Brodsky, 2021: Future changes in Northern Hemisphere summer weather persistence linked to projected Arctic warming. *Geophys. Res. Lett.*, **48**, e2020GL091603, https://doi.org/10.1029/2020GL091603.

Kossin, J. P., 2018: A global slowdown of tropical-cyclone translation speed. *Nature*, **558**, 104–107, https://doi.org/10.1038/s41586-018-0158-3.

Li, J., and D. W. J. Thompson, 2021: Widespread changes in surface temperature persistence under climate change. *Nature*, **599**, 425–430, https://doi.org/10.1038/s41586-021-03943-z.

Masato, G., B. J. Hoskins, and T. Woollings, 2013: Winter and summer Northern Hemisphere blocking in CMIP5 models. *J. Climate*, **26**, 7044–7059, https://doi.org/10.1175/JCLI-D-12-00466.1.

Matsueda, M., and H. Endo, 2017: The robustness of future changes in Northern Hemisphere blocking: A large ensemble projection with multiple sea surface temperature patterns. *Geophys. Res. Lett.*, **44**, 5158–5166, https://doi.org/10.1002/2017GL073336.

McKitrick, R., and J. Christy, 2020: Pervasive warming bias in CMIP6 tropospheric layers. *Earth Space Sci.*, **7**, e2020EA001281, https://doi.org/10.1029/2020EA001281.

Mesquita, M. D. S., D. E. Atkinson, I. Simmonds, K. Keay, and J. Gottschalck, 2009: New perspectives on the synoptic development of the severe October 1992 Nome storm. *Geophys. Res. Lett.*, **36**, L13808, https://doi.org/10.1029/2009GL038824.

Neu, U., and Coauthors, 2013: IMILAST: A community effort to intercompare extratropical cyclone detection and tracking algorithms. *Bull. Amer. Meteor. Soc.*, **94**, 529–547, https://doi.org/10.1175/BAMS-D-11-00154.1.

Perlwitz, J., M. Hoerling, and R. Dole, 2015: Arctic tropospheric warming: Causes and linkages to lower latitudes. *J. Climate*, **28**, 2154–2167, https://doi.org/10.1175/JCLI-D-14-00095.1.

Pfleiderer, P., C.-F. Schleussner, K. Kornhuber, and D. Coumou, 2019: Summer weather becomes more persistent in a 2°C

world. *Nat. Climate Change*, **9**, 666–671, https://doi.org/10.1038/s41558-019-0555-0.

Pinto, J. G., U. Ulbrich, G. C. Leckebusch, T. Spangehl, M. Reyers, and S. Zacharias, 2007: Changes in storm track and cyclone activity in three SRES ensemble experiments with the ECHAM5/MPI-OM1 GCM. *Climate Dyn.*, **29**, 195–210, https://doi.org/10.1007/s00382-007-0230-4.

Po-Chedley, S., B. D. Santer, S. Fueglistaler, M. D. Zelinka, P. J. Cameron-Smith, J. F. Painter, and Q. Fu, 2021: Natural variability contributes to model–satellite differences in tropical tropospheric warming. *Proc. Natl. Acad. Sci. USA*, **118**, e2020962118, https://doi.org/10.1073/pnas.2020962118.

Priestley, M. D. K., and J. L. Catto, 2022: Future changes in the extratropical storm tracks and cyclone intensity, wind speed, and structure. *Wea. Climate Dyn.*, **3**, 337–360, https://doi.org/10.5194/wcd-3-337-2022.

——, D. Ackerley, J. L. Catto, K. I. Hodges, R. E. McDonald, and R. W. Lee, 2020: An overview of the extratropical storm tracks in CMIP6 historical simulations. *J. Climate*, **33**, 6315–6343, https://doi.org/10.1175/JCLI-D-19-0928.1.

Raible, C. C., P. M. Della-Marta, C. Schwierz, H. Wernli, and R. Blender, 2008: Northern Hemisphere extratropical cyclones: A comparison of detection and tracking methods and different reanalyses. *Mon. Wea. Rev.*, **136**, 880–897, https://doi.org/10.1175/2007MWR2143.1.

Roberts, E., N. Nawri, and R. E. Stewart, 2008: On the storms passing over southern Baffin Island during autumn 2005. *Arctic*, **61**, 309–321, https://doi.org/10.14430/arctic27.

Scaife, A. A., T. Woollings, J. Knight, G. Martin, and T. Hinton, 2010: Atmospheric blocking and mean biases in climate models. *J. Climate*, **23**, 6143–6152, https://doi.org/10.1175/2010JCLI3728.1.

Schemm, S., 2023: Toward eliminating the decades-old "too zonal and too equatorward" storm-track bias in climate models. *J. Adv. Model. Earth Syst.*, **15**, e2022MS003482, https://doi.org/10.1029/2022MS003482.

Schiemann, R., and Coauthors, 2020: Northern Hemisphere blocking simulation in current climate models: Evaluating progress from the Climate Model Intercomparison Project Phase 5 to 6 and sensitivity to resolution. *Wea. Climate Dyn.*, **1**, 277–292, https://doi.org/10.5194/wcd-1-277-2020.

Schwierz, C., M. Croci-Maspoli, and H. C. Davies, 2004: Perspicacious indicators of atmospheric blocking. *Geophys. Res. Lett.*, **31**, L06125, https://doi.org/10.1029/2003GL019341.

Serreze, M. C., J. Voveris, A. P. Barrett, S. Fox, P. D. Blanken, and A. Crawford, 2022: Characteristics of extreme daily precipitation events over the Canadian Arctic. *Int. J. Climatol.*, **42**, 10 353–10 372, https://doi.org/10.1002/joc.7907.

Simpson, I. R., K. A. McKinnon, F. V. Davenport, M. Tingley, F. Lehner, A. A. Fahad, and D. Chen, 2021: Emergent constraints on the large scale atmospheric circulation and regional hydroclimate: Do they still work in CMIP6 and how much can they actually constrain the future? *J. Climate*, **34**, 6355–6377, https://doi.org/10.1175/JCLI-D-21-0055.1.

Smith, D. M., and Coauthors, 2019: The Polar Amplification Model Intercomparison Project (PAMIP) contribution to CMIP6: Investigating the causes and consequences of polar amplification. *Geosci. Model Dev.*, **12**, 1139–1164, https://doi.org/10.5194/gmd-12-1139-2019.

——, and Coauthors, 2022: Robust but weak winter atmospheric circulation response to future Arctic sea ice loss. *Nat. Commun.*, **13**, 727, https://doi.org/10.1038/s41467-022-28283-y.

Song, J.-N., G. Fu, Y. Xu, Z.-Y. Han, Q.-Z. Sun, and H. Wang, 2021: Assessment of the capability of CMIP6 global climate models to simulate Arctic cyclones. *Adv. Climate Change Res.*, **12**, 660–676, https://doi.org/10.1016/j.accre.2021.07.007.

Sun, Y., Z. Zhong, T. Li, L. Yi, and Y. Shen, 2021: The slowdown tends to be greater for stronger tropical cyclones. *J. Climate*, **34**, 5741–5751, https://doi.org/10.1175/JCLI-D-20-0449.1.

Tamarin, T., and Y. Kaspi, 2017: The poleward shift of storm tracks under global warming: A Lagrangian perspective. *Geophys. Res. Lett.*, **44**, 10 666–10 674, https://doi.org/10.1002/2017GL073633.

Tamarin-Brodsky, T., and Y. Kaspi, 2017: Enhanced poleward propagation of storms under climate change. *Nat. Geosci.*, **10**, 908–913, https://doi.org/10.1038/s41561-017-0001-8.

Tokarska, K. B., M. B. Stolpe, S. Sippel, E. M. Fischer, C. J. Smith, F. Lehner, and R. Knutti, 2020: Past warming trend constrains future warming in CMIP6 models. *Sci. Adv.*, **6**, eaaz9549, https://doi.org/10.1126/sciadv.aaz9549.

Ulbrich, U., G. C. Leckebusch, and J. G. Pinto, 2009: Extra-tropical cyclones in the present and future climate: A review. *Theor. Appl. Climatol.*, **96**, 117–131, https://doi.org/10.1007/s00704-008-0083-8.

Wills, R. C. J., R. H. White, and X. J. Levine, 2019: Northern Hemisphere stationary waves in a changing climate. *Curr. Climate Change Rep.*, **5**, 372–389, https://doi.org/10.1007/s40641-019-00147-6.

Woollings, T., and Coauthors, 2018: Blocking and its response to climate change. *Curr. Climate Change Rep.*, **4**, 287–300, https://doi.org/10.1007/s40641-018-0108-z.

Yamaguchi, M., J. C. L. Chan, I.-J. Moon, K. Yoshida, and R. Mizuta, 2020: Global warming changes tropical cyclone translation speed. *Nat. Commun.*, **11**, 47, https://doi.org/10.1038/s41467-019-13902-y.

Ye, K., and G. Messori, 2021: Inter-model spread in the wintertime Arctic amplification in the CMIP6 models and the important role of internal climate variability. *Global Planet. Change*, **204**, 103543, https://doi.org/10.1016/j.gloplacha.2021.103543.

Zappa, G., L. C. Shaffrey, and K. I. Hodges, 2013: The ability of CMIP5 models to simulate North Atlantic extratropical cyclones. *J. Climate*, **26**, 5379–5396, https://doi.org/10.1175/JCLI-D-12-00501.1.

Zolina, O., and S. K. Gulev, 2002: Improving the accuracy of mapping cyclone numbers and frequencies. *Mon. Wea. Rev.*, **130**, 748–759, https://doi.org/10.1175/1520-0493(2002)130<0748:ITAOMC>2.0.CO;2.